

ISOCAM Observations of Normal Star-Forming Galaxies: The Key Project Sample¹

D.A. Dale,² N.A. Silberman,² G. Helou,² E. Valjavec,² S. Malhotra,² C.A. Beichman,²
J. Brauher,² A. Contursi,² H. Dinerstein,³ D. Hollenbach,⁴ D. Hunter,⁵ S. Kolhatkar,²
K.Y. Lo,⁶ S. Lord,² N.Y. Lu,² R. Rubin,⁴ G. Stacey,⁷ H. Thronson, Jr.,⁸ M. Werner,⁹ H.
Corwin²

ABSTRACT

We present mid-infrared maps and preliminary analysis for 61 galaxies observed with the *Infrared Space Observatory*. Many of the general features of galaxies observed at optical wavelengths—spiral arms, disks, rings, and bright knots of emission—are also seen in the mid-infrared, except the prominent optical bulges are absent at 6.75 and 15 μm . In addition, the maps are quite similar at 6.75 and 15 μm , except for a few cases where a central starburst leads to lower $\frac{I_\nu(6.75\mu\text{m})}{I_\nu(15\mu\text{m})}$ ratios in the inner region. We also present infrared flux densities and mid-infrared sizes for these galaxies. The mid-infrared color $\frac{I_\nu(6.75\mu\text{m})}{I_\nu(15\mu\text{m})}$ shows a distinct trend with the far-infrared color $\frac{I_\nu(60\mu\text{m})}{I_\nu(100\mu\text{m})}$. The quiescent galaxies in our sample ($\frac{I_\nu(60\mu\text{m})}{I_\nu(100\mu\text{m})} \lesssim 0.6$) show $\frac{I_\nu(6.75\mu\text{m})}{I_\nu(15\mu\text{m})}$ near unity, whereas this ratio drops significantly for galaxies with higher global heating intensity levels. Azimuthally-averaged surface brightness profiles indicate the

¹This paper is based on observations with the Infrared Space Observatory (*ISO*). *ISO* is an ESA project with instruments funded by ESA member states (especially the PI countries: France, Germany, The Netherlands and the United Kingdom) and with the participation of ISAS and NASA.

²IPAC, California Institute of Technology, MS 100-22, Pasadena, CA 91125

³University of Texas, Astronomy Dept. RLM 15.308, Austin, TX 78712

⁴NASA/Ames Research Center, MS 245-6, Moffett Field, CA 94035

⁵Lowell Obs., 1400 Mars Hill Rd., Flagstaff, AZ 86001

⁶University of Illinois, Astronomy Dept. 1002 W. Green St. Urbana, IL 61801

⁷Cornell University, Astronomy Dept., 220 Space Science Building, Ithaca, NY 14853

⁸NASA HQ Code SR, 300 E. St. SW, Washington D.C. 20024

⁹Jet Propulsion Laboratory, MS 233-303, 4800 Oak Grove Rd., Pasadena, CA 91109

extent to which the mid-infrared flux is centrally concentrated, and provide information on the radial dependence of mid-infrared colors. The galaxies are mostly well resolved in these maps: almost half of them have $< 10\%$ of their flux in the central resolution element. A comparison of optical and mid-infrared isophotal profiles indicates that the optical flux at 4400 \AA near the optical outskirts of the galaxies is approximately eight (seven) times that at $6.75 \text{ }\mu\text{m}$ ($15 \text{ }\mu\text{m}$), comparable with observations of the diffuse quiescent regions of the Milky Way.

Subject headings: galaxies: ISM — galaxies: general — galaxies

1. Introduction

Normal galaxies, defined as those with on-going star formation, account for most of the luminous mass in the local Universe. Their luminosity is derived from stars and they span a broad range of observed morphologies, luminosities, and infrared-to-blue ratios. Results from *IRAS* have shown that the infrared colors from the four *IRAS* bands are sensitive indices of the radiation intensity in the interstellar medium. The mid-infrared ($5\text{--}20 \text{ }\mu\text{m}$) emission is dominated by very small grains fluctuating to high temperatures and polycyclic aromatic hydrocarbons (PAHs) (Helou et al. 2000). These grains are not in thermal equilibrium but they still convert heating photons and thereby trace star formation. Larger grains in thermal equilibrium dominate the emission from normal galaxies at longer wavelengths. By comparing the mid-infrared emission to other components of the galaxy such as H I, H_2 , ionized gas, and starlight, one can derive the physical properties of the interstellar gas, dust and radiation field in galaxies (e.g. Vigroux et al. 1999).

The *Infrared Space Observatory* (*ISO*) U.S. Key Project on Normal Galaxies (PI: G. Helou, proposal id: SF_GLX_*, hereafter the “Key Project”) was proposed to study the interstellar medium of a broad range of normal galaxies using three of the four instruments aboard *ISO*: ISOCAM, ISOLWS, and ISOPHOT. Under NASA guaranteed time, the U.S. Key Project obtained *ISO* observations of 69 galaxies. Nine relatively nearby and extended galaxies were chosen to provide spatially resolved cases so that various phases of the interstellar medium could be studied independently. The remaining 60 galaxies in the Key Project sample cover the full range of observed morphologies, luminosities, and *IRAS* colors seen in normal galaxies. Using this diverse sample, we hope to gain new insight into the star formation process on the scale of galaxies, especially its drivers and inhibitors (Helou et al. 1996).

2. The U.S. Key Project ISOCAM Sample

The CAM sample of galaxies for the Key Project is presented in Table 1 where we list each galaxy's position, optical size, morphology, recession velocity, distance estimate, and far-infrared-to-blue ratio. The positions, optical sizes, and velocities come from the NASA Extragalactic Database¹⁰ and were last updated February 2000. The distances were computed in the Local Group reference frame assuming a Hubble constant of $75 \text{ km s}^{-1} \text{ Mpc}^{-1}$. The mean distance of the sample is 34 Mpc. The RC3 (de Vaucouleurs et al. 1991) optical morphological classification for each galaxy was kindly re-examined by H. Corwin using the POSS plates and more recent CCD observations by the Key Project team and those found in the literature; we have updated a total of 17 RC3 morphologies. Figure 1 shows the histogram of optical morphological types. The morphologies are lenticular or later except for one elliptical, NGC 6958. There is an approximately even distribution of spirals and a large number of irregulars in the final sample.

In all, five relatively extended galaxies and 56 smaller galaxies were mapped with ISOCAM as part of the Key Project. These galaxies span a broad range in physical properties such as total luminosity, dust temperature, and star formation activity. Figure 2 is a color-color diagram of ratios of *IRAS* flux densities for the sample (see Table 4). Quiescent galaxies such as NGC 7418 lie along the upper left of the distribution while more active star forming galaxies such as NGC 1569 are found to the lower right.

3. The CAM Observations

Observations were made using the 32×32 pixel Si:Ga long wavelength (LW) array of ISOCAM (Césarsky et al. 1996) aboard ISO (Kessler et al. 1996). We utilized the narrow-band LW1 filter ($4.5 \mu\text{m}$, $\delta\lambda = 1.0 \mu\text{m}$), the broad-band LW2 filter ($6.75 \mu\text{m}$, $\delta\lambda = 3.5 \mu\text{m}$), and broad-band LW3 filter ($15.0 \mu\text{m}$, $\delta\lambda = 6.0 \mu\text{m}$) to sample the mid-infrared emission from the galaxies. The mid-infrared regime represents a transition from stellar to interstellar emission, though the former should be negligible at $6.75 \mu\text{m}$ for the majority of our sample. From ISOPHOT observations (Helou et al. 2000) we know there are strong aromatic emission features at 6.2 , 7.7 and $8.6 \mu\text{m}$, all of which fall within the $6.75 \mu\text{m}$ filter. The $15 \mu\text{m}$ filter contains some emission from aromatics at 11.3 and $12 \mu\text{m}$, and continuum emission from very small grains. We note that strong [Ne II] ($12.8 \mu\text{m}$)

¹⁰The NASA/IPAC Extragalactic Database is operated by the Jet Propulsion Laboratory, California Institute of Technology, under contract with the National Aeronautics and Space Administration.

and [Ne III] ($15.6\ \mu\text{m}$) fine structure lines have been observed in the spectra of H II regions (e.g. M17; Césarsky et al. 1996). Rotational H_2 lines are also seen in the LW3 bandpass (Kunze et al. 1996, Valentijn et al. 1996, Timmerman et al. 1996), and while these lines are important physically, their contribution to the total flux is very small (Helou et al. 2000).

All of our ISOCAM observations used a gain setting of 2 and a $6'' \times 6''$ pixel field of view. Tables 2 and 3 list the date, revolution (orbit number during the *ISO* mission), and exposure times for each galaxy. For six galaxies (NGC 1313, NGC 3620, NGC 5713, IC 4595, NGC 6753, NGC 7771), the $4.5\ \mu\text{m}$ observations were not done at the same time as the 6.75 and $15\ \mu\text{m}$ observations, so the $4.5\ \mu\text{m}$ maps for these galaxies are at a different roll angle compared to the 6.75 and $15\ \mu\text{m}$ maps.

The bulk of our ISOCAM observations are in the form of 2×2 raster maps (Table 2) with a raster step of $75''$, or 12.5 pixel widths. This allows us to resample the resulting maps onto a finer grid with $3''$ per pixel. The final maps are $4'.45 \times 4'.45$. Five galaxies have larger raster maps (Table 3), with up to 8×8 pointings and a step size of $81''$, or 13.5 pixel widths, which again allow us to rebin the final maps onto a $3''\ \text{pixel}^{-1}$ grid.

4. Data Reduction

The CAM observations were reduced using the CAM Interactive Analysis (CIA) software package (Delaney 1998) using Pipeline 7 datasets. The reduction steps include dark subtraction, deglitching, transient removal, and flat-field correction. We experimented with various methods for each step, with the goal of finding a reduction method that worked well for the entire galaxy sample.

The arrival of the first wave of ISOCAM observations in mid-1996 allowed us to explore in some detail various reduction and analysis techniques. This early work indicated that the library dark distributed with each dataset did an acceptable job in removing the effects of the dark current. The default deglitcher, which uses the multi-resolution median transform method (Starck et al. 1999), did the best job in removing the transitory cosmic ray and charged particle hits without simultaneously flagging the source data as bad data. Library sky flats from some revolutions have cosmic-ray/charged particle residuals, so we investigated how to use the observations themselves to create a target field sky flat. We found that as long as the galaxy is not too extended or too bright, we could create a good sky flat from the target field data. The only remaining task was to remove the effects of the finite response time, which can artificially increase or decrease flux detections, referred to below as “transient removal.”

All transient removal techniques that existed within CIA circa 1997 were tested to identify the one best suited for our type of observations. In particular, we studied in detail the relative merits of the 'fit3,' 'inverse,' and 'fouks-schubert' methods. All other options—dark, deglitcher, target field sky flat—were unchanged in the tests. Individual pixels from both on and off-source observations were examined before and after transient removal, and the final maps were inspected. The 'fit3' (Siebenmorgen et al. 1997) method appeared to do the best job but it leaves the first raster position, the one most affected by the transient, at a slightly different flux level than the remaining raster positions. This is because 'fit3' removes the transient effect independently for each raster position. Thus, the average map from each raster position will have a slightly different sky value, with the first raster position being more discrepant (usually by more than 5%) compared to the remaining raster positions. To solve this problem, we experimented with masking out the first raster position. Several of the transient removal methods were re-tested, and again the 'fit3' method appeared to work best in terms of removing the transient from individual pixels, both on and off-source, and producing a "good" final map.

In summary, the data reduction steps we use were as follows. First, starting with the Standard Processed Data (SPD) of the pipeline processing, a library dark is subtracted from each frame. Next, each frame is deglitched using the multi-resolution median transform method. Then all of the frames in the first raster position are masked out (not used to produce the final map). Next, transients are removed using the Saclay 'fit3' model. The frames from each raster position are averaged together, and then these average images are used to make a target field sky flat. For the $4.5\ \mu\text{m}$ maps the library sky flat was used, as the sky flux in these maps is too low to produce good target field sky flats from the data. Next, the flat-fielded average images are mosaicked to create the final map. The final step converts the pixel units from ADU/gain/second to mJy.

5. The CAM Images

5.1. The Small Maps

Figure 3 presents optical Digitized Sky Survey (DSS) images and ISOCAM maps for the 2×2 raster sample of galaxies, arranged one row per galaxy. Figures 4-8 present the larger raster maps, also including the optical DSS images for comparison. As a consequence of the 'dead' column #24 in the CAM LW array, all of the maps contain two zero value columns towards their right edge. There is also a notch in the lower left corner of the ISOCAM maps, due to our masking of the first raster position. In many cases the maps still show low level residuals due to transients from the sources. In particular, residuals just

below the source are common and result from the source being in that position during the third raster observation. There are also weak residuals in some maps from the second raster position (the upper left in the ISOCAM maps). These residuals are due to our scheme of masking the first raster position, as they are very weak or non-existent in maps made with all four raster positions. Such low level residuals are masked out before source fluxes are measured.

NGC 4490 and UGC 2855 are relatively large galaxies compared to the $4'45 \times 4'45$ raster maps; for both galaxies the amount of sky area in the final maps is insufficient. We tried using sky flats from the observations themselves and the library sky flats. The results using the library sky flats are superior to the target field sky flats, leaving very weak transient residuals and a much smoother sky. The library sky flats do not appear to add any artifacts to the final maps (as was the case for a few of our galaxies during the testing of reduction methods), and so for these two galaxies fluxes are determined from ISOCAM maps reduced using library sky flats. We note that the ISOCAM map of NGC 4490 does not contain the entire galaxy; our 6.75 and 15 μm fluxes should be considered lower limits for this galaxy.

We successfully detected all galaxies at all mid-infrared wavelengths attempted in our ISOCAM program, (though just barely for two nearby galaxies; see §5.2.3). Overall the CAM maps show many of the same features present in the optical images; prominent spiral arms or rings, and distinct clumps and regions of relatively high mid-infrared emission are quite evident in some of the later type galaxies such as IC 4595, NGC 1385, NGC 3705, NGC 4713, NGC 7418, and UGC 2855. However, in most cases the bulges seen in the optical are not apparent in the mid-infrared maps. More importantly, the mid-infrared morphologies at 4.5, 6.75, and 15 μm are qualitatively similar. There are no obvious differences in how the light is distributed, though upon closer inspection of the central regions of some galaxies there are hints of variations with wavelength. A quantitative look at the relative distribution of mid-infrared emission at 6.75 and 15 μm will be presented in Section 7.1. The typical sky background levels are 1, 5, and 20 MJy sr^{-1} , with rms fluctuations at the 0.1, 0.1, and 0.2 MJy sr^{-1} levels, at 4.5, 6.75, and 15 μm , respectively.

5.2. The Larger Maps

5.2.1. IC 10

IC 10 was observed twice. In the first set of observations the center of the galaxy was chosen to be the center of the map, as with the maps for all our other galaxies. However,

we noticed that the mid-infrared emission from IC 10 extended more to the west of center, leaving some interesting structure on the edges of the maps. A second set of observations was taken a year later to more properly map the mid-infrared emission. The final set of 6.75 and 15 μm maps results from a co-add of the maps from the two epochs. The 11.4 μm (LW8 filter) and 4.5 μm maps were obtained only in the second epoch.

In the mid-infrared IC 10 appears to consist of a collection of bright knots, except at 4.5 μm where the galaxy appears to be quite faint. IC 10 is classified as a barred irregular galaxy but the bar is not apparent in the mid-infrared maps. There are two wispy arms extending to the north which contain distinct knots of stronger mid-infrared emission. An overall faint and diffuse mid-infrared emission is detected towards the west and south of the galaxy center, extending almost to the edge of our maps. A surface brightness analysis of the 6.75 and 15 μm ISOCAM observations of IC 10 can be found in Dale et al. (1999).

5.2.2. *NGC 1313*

Observations for this galaxy were taken in two parts, a western piece and an eastern piece, with the two pieces mosaicked together to make a final map. The 4.5 μm observation was taken 5 months later at a different roll angle. In the mid-infrared, the bar of the galaxy appears as discrete emission sources. The spiral arms are prominent as both diffuse emission and knots of strong emission. Similar to what is seen optically, there is also a faint wisp of emission directly to the south of galaxy center. The bright knots of optical emission in the eastern arm also show strongly in the mid-infrared. Our ISOCAM map is unfortunately too small to cover the large star-forming complex just to the southwest of the galaxy (Ryder et al. 1995). The galaxy is barely detected at 4.5 μm . A surface brightness analysis of the 6.75 and 15 μm observations of NGC 1313 can be found in Dale et al. (1999).

5.2.3. *NGC 2366 and NGC 6822*

NGC 2366 and NGC 6822 are low luminosity irregulars that contain several moderate to supergiant-sized H II regions (Hunter et al. 2000). The mid-infrared maps for these galaxies are of insufficient depth: the 1σ rms fluctuations in the sky level for NGC 2366 are 0.05 and 0.14 MJy sr⁻¹ at 6.75 and 15 μm , respectively, while the numbers for NGC 6822 are 0.09 and 0.28 MJy sr⁻¹. Alternatively, very little 6.75 or 15 μm emission is detected from these two galaxies, suggesting they contain only a small amount of dust. In NGC 2366 most of the mid-infrared emission coincides with the supergiant H II region NGC

2363 in the southwestern part of the galaxy. There is a much fainter region of emission to the northeast of that which does not obviously correspond to anything in particular in the optical. In NGC 6822 the mid-infrared emission is found in four H II regions. There is a bit of diffuse emission towards the center of the galaxy, but it is of too low signal-to-noise to measure with any degree of confidence. The fluxes given in Table 4 are the combined fluxes of the H II regions; we caution that these are only estimates of the total flux, as the true sizes of the galaxies in the mid-infrared are difficult to determine. There are a few foreground stars seen in the $6.75\ \mu\text{m}$ maps.

5.2.4. NGC 6946

At optical wavelengths, NGC 6946 is a striking example of a nearly face-on ($i \sim 30^\circ$) spiral galaxy. The galaxy is equally rich in detail in the mid-infrared. The spiral arms can easily be traced in the mid-infrared maps, and each contains several knots of brighter emission. The ‘sharp’ edge of the northeastern-most arm is real and not an artifact of the mosaicking. It is also seen in *IRAS* HiReS maps of NGC 6946. Preliminary work on NGC 6946 from these ISOCAM observations (using earlier data reduction techniques) by Helou et al. (1996) indicated that there is very little mid-infrared color variation throughout the disk of the galaxy. This result is echoed by the work of Tuffs et al. (1996), who used ISOPHOT data to suggest that the bulk of the far-infrared luminosity is due to a uniformly colored and rather cold diffuse emission from the disk. Work by Malhotra et al. (1996), again using these same CAM observations reduced with prior techniques, showed that the mid-infrared emission is consistent with an exponential disk of scale length of $75''$, the flux profile computed from the median flux within annuli between 70 and $200''$. They also indicate that the mid-infrared arm-interarm contrast, being close to that observed in R -band but lower than observed in $H\alpha$, suggests that non-ionizing radiation plays an important role in the heating of the dust. A surface brightness analysis of the ISOCAM observations for NGC 6946, using our new reduction methods, can be found in Dale et al. (1999). We stress that the main results do not change: the color variations analyzed in Dale et al. are quite close to those presented earlier. In fact, the small discrepancies ($\sim 10\%$) between the two analyses can be taken as a first-order estimate of the uncertainties in the data. Moreover, using the newly-processed data we find a similar mid-infrared disk scale length ($72''$). Finally, we point out that the starbursting center is quite bright in the mid-infrared; our integration times nearly saturated two pixels at $15\ \mu\text{m}$ and saturated as many as four pixels at $6.75\ \mu\text{m}$. The impact of these saturated and nearly saturated pixels on the overall flux density is measurably small, approximately a 15% (25%) effect at 15 (6.75) μm for affected pixels (the method used to approximate this effect is described in

Section 6.1). Our values for the total flux density should be formally taken as lower limits, though the underestimation is no more than a few percent.

6. Flux Density Estimates

Before beginning any quantitative analysis on the ISOCAM images presented in Figures 3-8, we cleaned the images by masking any foreground stars and cosmic ray/transient residuals. To allow direct comparison between the various filters we smoothed the maps to a similar resolution. To do this we needed to first estimate the approximate resolution for the 6.75 and 15 μm maps. There are a few maps which have strong emission from a foreground star (e.g. NGC 1569 and NGC 6946), and several galaxies appear to be unresolved at these mid-infrared wavelengths (*IRAS* F10565, NGC 4418, IC 860, IC 883, CGCG1510, *IRAS* F23365, Markarian 331). Analysis of these images indicate a (FWHM) resolution of $\sim 7''$ and $\sim 8''$ at 6.75 and 15 μm , respectively. This information was used to convolve the 6.75 and 15 μm maps, using slightly different Gaussian smoothing profiles for each filter, to generate maps with approximately uniform resolution ($9''$ FWHM). As a final step the images were registered to the coordinate system of the 15 μm map by assuming the peak emission at 6.75 μm is spatially coincident with the peak emission at 15 μm .

6.1. Mid-Infrared Flux Densities

Multi-aperture photometry is our preferred method for extracting mid-infrared flux densities. For each galaxy care is taken to define the apertures and background annulus using the flux density distribution from both the 6.75 and 15 μm (and when available the 4.5 μm) maps. In each case, a series of evenly spaced, concentric apertures are centered on the central emission peak, with the outermost aperture sized according to the greatest extent of the emission in either map. The background annulus was then defined starting from the outermost aperture, unless a localized contamination (e.g. star) warrants starting the background annulus at a slightly larger radius; the typical background annulus has a width of $15''$. The mean value within the background annulus is taken to be the sky background level. The background-subtracted flux density within the outermost aperture is the total flux density.

The mid-infrared flux densities and their uncertainties for the galaxies are given in Table 4 along with the *IRAS* flux densities. Column 1 in Table 4 lists the galaxy. Columns 2-5 list the *IRAS* flux densities in Janskys and columns 6-7 list the *ISO* 6.75 and 15 μm

flux densities and their uncertainties in Jy (see §6.2 for a comparison of ISOCAM and *IRAS* 12 μm fluxes). We assume a 20% uncertainty in the flux density calibration of ISOCAM data (Blommaert & Cesarsky 1998; Biviano 1998). By far, this uncertainty level dominates any other uncertainties that are introduced by our method of flux density extraction (e.g. choice of aperture and background annulus, sky rms fluctuation, etc.). However, our finite aperture measurements systematically underestimate the total flux density of the galaxies by a small amount due to the limiting $\sim 0.1 \text{ MJy sr}^{-1}$ sensitivity of our observations. We can estimate the amount of low surface brightness emission that is missed by extrapolating the observed isophotal surface brightness trends. Assuming such trends hold out to a surface brightness of $0.001 \text{ MJy sr}^{-1}$ (about two disk scale-lengths), no more than a few percent of the flux is missing. Overall, for most galaxies we thus find a total flux density uncertainty of 20%; this number is slightly higher ($\sim 25\%$) for about one fourth of the sample due to more significant sky background fluctuations.

The uncertainty is slightly larger in cases where i) the mid-infrared emission extends beyond the observed target field, or ii) there is saturation, two additional effects that systematically lower the flux density measure. Only the fluxes for UGC 2855 and NGC 4490 suffer from the former effect; extrapolations of the observed profiles, as described above, show we are missing $\lesssim 5\%$ of such flux for these two galaxies. A second concern is that observations of a few galaxies saturated the analog to digital converter for a small number of pixels, the effect being more serious for the longer elementary integrations for the $6.75 \mu\text{m}$ bandpass. We have gauged the amplitude of this effect using the known response function of the ISOCAM detectors: the actual flux density should be larger than the initial frame's measure by a factor $1/0.6$ (ISOCAM Observer's Manual). For most of the 11 galaxies exhibiting saturated pixels the net effect is an underestimate of the total flux density by 6% or less; the 6.75 and $15 \mu\text{m}$ flux densities for NGC 4418 are underestimated by about 15% and 25%, respectively, comparable to the calibration uncertainty level. The flux densities computed for these galaxies are lower limits and are indicated by a colon in Table 4; they may be assumed to be uncertain at the 25% level.

Table 5 lists the total $4.5 \mu\text{m}$ flux densities for 13 galaxies in our sample. For NGC 1569 we obtained 2×2 ISOCAM maps in eight filters; NGC 1569 flux densities and uncertainties are given in Table 6. The typical LW1 flux density uncertainty is 25-30% due to a lower overall signal to noise compared to the LW2 and LW3 maps.

6.2. Calibration Check: The Consistency of *ISO* and *IRAS* Fluxes

An independent check of the calibration of our ISOCAM maps can be provided by *IRAS* data. Figure 9 presents the ratio of ISOCAM fluxes to *IRAS* 12 μm fluxes versus $\frac{I_\nu(60\mu\text{m})}{I_\nu(100\mu\text{m})}$ color. The dashed lines indicate the expected mid-infrared to 12 μm ratio for cirrus ($\log \frac{I_\nu(6.75\mu\text{m})}{I_\nu(12\mu\text{m})} = -0.29$ and $\log \frac{I_\nu(15\mu\text{m})}{I_\nu(12\mu\text{m})} = -0.01$ for ρ Ophiuchi; W. Reach, private communication). The expected cirrus color agrees well with our observed $\frac{I_\nu(6.75\mu\text{m})}{I_\nu(12\mu\text{m})}$ color ratio: $\log \frac{I_\nu(6.75\mu\text{m})}{I_\nu(12\mu\text{m})} [-0.5 < \log \frac{I_\nu(60\mu\text{m})}{I_\nu(100\mu\text{m})} < -0.2] = -0.26 \pm 0.11$ (the uncertainty represents the population dispersion excluding NGC 1155 and NGC 6958). The agreement is even better for the more quiescent galaxies, even though real galaxies have other emission (star-formation regions) in them in addition to cirrus. Moreover, we expect the $\frac{I_\nu(6.75\mu\text{m})}{I_\nu(12\mu\text{m})}$ color to decrease for warmer galaxies (relatively high $\frac{I_\nu(60\mu\text{m})}{I_\nu(100\mu\text{m})}$ color) since the PAH features in the 6.75 μm filter become relatively weak compared to the rising continuum in the 12 μm band, and this is indeed observed. Photospheres can contribute to the flux at 6.75 μm and throw off the ratio, especially for measurements of elliptical galaxies. Since this effect does not seem significant in this sample, we conclude that in most of our sample the 6.75 μm and longer wavelength bands are dominated by interstellar emission.

For the $\frac{I_\nu(15\mu\text{m})}{I_\nu(12\mu\text{m})}$ color ratio comparison with cirrus, the agreement is not as good, but the ratio observed for galaxies is lower than that of cirrus only by 35%: $\log \frac{I_\nu(15\mu\text{m})}{I_\nu(12\mu\text{m})} [-0.5 < \log \frac{I_\nu(60\mu\text{m})}{I_\nu(100\mu\text{m})} < -0.2] = -0.14 \pm 0.10$ (excluding NGC 6958). Surprisingly, the offset goes in the wrong direction for astrophysical effects to resolve the discrepancy: the 15 μm band should pick up more emission in galaxies than the cirrus spectrum represents, and we reach the “cirrus ratio” only for mildly active galaxies. There are a few possible explanations for this discrepancy, most importantly the uncertainty in the cirrus spectrum (calibration uncertainty and spatial variations in the cirrus behavior), the uncertainties in the various filter band passes, and incompleteness in the *ISO* flux integral. The *ISO* 15 μm maps are integrated only down to the ~ 0.2 MJy sr^{-1} isophote, whereas the large angular size of the *IRAS* detectors tended to pick up contributions from extended diffuse emission. However, as pointed out in Section 6.1, extrapolations of the observed surface brightness profiles down to 0.001 MJy sr^{-1} show we are missing at most 5% of the total *ISO* flux. Moreover, if the problem is *ISO* flux incompleteness, we might expect a similar discrepancy in the $\frac{I_\nu(6.75\mu\text{m})}{I_\nu(12\mu\text{m})}$ comparison: the *ISO* 6.75 μm maps go only slightly deeper, to ~ 0.1 MJy sr^{-1} . We conclude that it is unlikely that *ISO* flux incompleteness is responsible.

7. Analysis

7.1. Mid-Infrared Flux Curve of Growth Profiles

Results of the aperture photometry described in Section 6.1 are presented in Figures 10 and 11. From the smoothed maps, the curve of growth profiles for the 6.75 and 15 μm emission are represented by the solid and dashed lines, respectively. Each profile is flux-normalized to the total flux observed in the respective filters. The bold, solid vertical line indicates the resolution scale in physical units and corresponds to the 4".5 HWHM Gaussian smoothing profile. The emission from most galaxies is very well resolved in the maps: for about half (45%) of the galaxies in our sample, 10% or less of the mid-infrared light arises from within the central ISOCAM beam; one-sixth of the galaxies emit $> 25\%$ in the central beam. While the physical extent and concentration of the mid-infrared emission varies from galaxy to galaxy, the 6.75 and 15 μm profiles are remarkably similar for a given source.

Against this general similarity, some galaxies display strong central $\frac{I_\nu(15\mu\text{m})}{I_\nu(6.75\mu\text{m})}$ ratios, which can be identified in Figure 10 by a narrower 15 μm than 7 μm curve. The most notable cases are NGC 1156, NGC 1569, NGC 4519, IC 4662, NGC 6958, and NGC 2366. As discussed below (Section 7.2), larger values of $\frac{I_\nu(15\mu\text{m})}{I_\nu(6.75\mu\text{m})}$ point to more intense heating of the dust, suggesting that the galaxies with this central color enhancement harbor high densities of H II regions in their centers, or nuclear starbursts. This is indeed consistent with the properties of NGC 1156, NGC 1569, IC 4662, and NGC 2366, which are all Magellanic Irregulars with bright star-forming regions near their centers (Hunter et al. 2000; Ho et al. 1995). It is interesting to note that the reverse situation, namely a decrease in the $\frac{I_\nu(15\mu\text{m})}{I_\nu(6.75\mu\text{m})}$ color, is not observed in this sample.

7.2. The *ISO-IRAS* Color Diagram

The $\frac{I_\nu(6.75\mu\text{m})}{I_\nu(15\mu\text{m})}$ ratio has emerged as an interesting diagnostic of the radiation environment (Helou et al. 1997). As evident in the *ISO-IRAS* color-color diagram (Figure 12), this ratio remains relatively constant and near unity as the interstellar medium of galaxies proceeds from quiescent to mildly active, where the level of activity is indicated by a rising $\frac{I_\nu(60\mu\text{m})}{I_\nu(100\mu\text{m})}$ (Helou 1986). As dust heating increases further, the flux at 15 μm increases steeply compared to 7 μm . The data plotted in Figure 12 are consistent with an inflection in the mean trend occurring near $\log \frac{I_\nu(60\mu\text{m})}{I_\nu(100\mu\text{m})} = -0.2$, which we interpret as due to excess emission in the 15 μm band rather than a drop in the 7 μm band. The main argument for this interpretation is that the $I_\nu(6.75\mu\text{m})/\text{FIR}$ ratio does not drop as precipitously as

$\frac{I_\nu(6.75\mu\text{m})}{I_\nu(15\mu\text{m})}$ for these objects. We assign to this emission a characteristic temperature $100\text{ K} < T_{\text{MIR}} < 200\text{ K}$, since that is the range that would allow a blackbody to contribute considerably to the $15\mu\text{m}$ band but not to the $7\mu\text{m}$ band; the estimates hold for modified blackbodies as well. Such values of T_{MIR} are typical of heating intensities about 10^4 times greater than the diffuse interstellar radiation field in the Solar Neighborhood (Helou et al. 1997). While such a temperature could result from classical dust heated within or just outside H II regions, there is no decisive evidence as to the size or location of grains involved or whether in fact they are in equilibrium with the radiation field. It is simpler at this time to associate this component empirically with the observed emission spectrum of H II regions and their immediate surroundings (Tran 1998; Contursi et al. 2000). This emission has severely depressed aromatic feature or PAH emission, and is dominated by a steeply rising though not quite a blackbody continuum near $15\mu\text{m}$, consistent with mild fluctuations in grain temperatures, $\Delta T/T \sim 0.5$. This H II region hot dust component characterized by color temperatures $100\text{ K} < T_{\text{MIR}} < 200\text{ K}$ becomes detectable in systems where the color temperature from the $\frac{I_\nu(60\mu\text{m})}{I_\nu(100\mu\text{m})}$ ratio is only $T_{\text{FIR}} \approx 50\text{ K}$ (Helou et al. 1988). This disparity between color temperatures derived from different wavelengths demonstrates the broad distribution of dust temperatures within any galaxy.¹¹ The combined data from *ISO* and *IRAS* on these systems are consistent with an extension of the “two-component model” of infrared emission (Helou 1986). The low $\frac{I_\nu(6.75\mu\text{m})}{I_\nu(15\mu\text{m})}$ ratio is associated with the active component, and combines in a variable proportion with a component with a $\frac{I_\nu(6.75\mu\text{m})}{I_\nu(15\mu\text{m})}$ near unity (Dale et al. 1999).

7.3. Mid-Infrared vs Optical Sizes

It is interesting to measure the size of a galaxy in the mid-infrared in comparison to an equivalent measure at optical wavelengths, e.g. $R(0.44\mu\text{m})_{25}$, the length of the semi-major axis out to 25 mag arcsec⁻² in *B* (obtained from the RC3 catalog; de Vaucouleurs et al. 1991). Using fits of isophotal ellipses to the mid-infrared distribution, we measure semi-major axis lengths from both the 6.75 and $15\mu\text{m}$ maps at several surface brightness levels between 0.2 and 1.0 MJy sr^{-1} . We fit elliptical isophotes to the mid-infrared images using both standard and customized IRAF packages (see Haynes et al. 1999 for further details on the GALPHOT surface photometry fitting routines). We do not measure sizes at lower surface brightness levels due to S/N constraints, since as discussed in Section

¹¹The quoted far-infrared color temperatures are merely approximations arising from graybody profiles that exhibit similar flux ratios for the two wavelength bands. See Helou et al. (1988) for more details on $\frac{I_\nu(60\mu\text{m})}{I_\nu(100\mu\text{m})}$ color temperatures.

5.1, the typical rms fluctuation in the sky background is $0.1 - 0.2 \text{ MJy sr}^{-1}$. The mid-infrared semi-major axes are corrected for ISOCAM resolution using a quadratic formula $R = \sqrt{R_{obs}^2 - 4''.5^2}$. The open circles in Figure 13 show the mean $R(6.75\mu\text{m})/R(0.44\mu\text{m})_{25}$ and mean $R(15\mu\text{m})/R(0.44\mu\text{m})_{25}$ for the sample as a function of the mid-infrared surface brightness level at which mid-infrared sizes are measured. Error bars reflect the one sigma population dispersions in the ratios at each surface brightness, divided by the square root of the number of galaxies; histograms of the ratios at each surface brightness level are also displayed at the top of the figure. The data are reasonably well approximated by an exponential dependence of mid-infrared surface brightness on radius, and the trend holds for the entire range of measured surface brightness levels. Invoking a small extrapolation of the trend to lower surface brightness levels shows that, on average, mid-infrared sizes at 6.75 and $15 \mu\text{m}$ match $R(0.44\mu\text{m})_{25}$ at a surface brightness level of $I_\nu(6.75\mu\text{m}) \approx 0.04 \text{ MJy sr}^{-1}$ and $I_\nu(15\mu\text{m}) \approx 0.09 \text{ MJy sr}^{-1}$ respectively. The uncertainties in these surface brightness estimates are 25%.

Since $R(0.44\mu\text{m})_{25}$ is comparable to the location of the Sun in the Milky Way, one would expect similar values of the mid-infrared surface brightness of the Milky Way in the Local Neighborhood. For a typical high Galactic latitude H I column density of $\sim 2 - 3 \times 10^{20} \text{ cm}^{-2}$ (Kulkarni & Heiles 1988), and for an emissivity of $4\pi\nu I_\nu(12\mu\text{m}) = 1.1 \times 10^{-31} \text{ W}$ per H atom (Boulanger & Péroult 1988), the expected mid-infrared brightness would be $I_\nu(12\mu\text{m}) \sim 0.08 \text{ MJy sr}^{-1}$, indeed comparable to the values above. In addition, one can translate the $12 \mu\text{m}$ band flux density into expected 6.75 and $15 \mu\text{m}$ flux densities using the cirrus spectrum of Reach and Boulanger (1998). One finds $I_\nu(6.75\mu\text{m}) \sim 0.04 \text{ MJy sr}^{-1}$ and $I_\nu(15\mu\text{m}) \sim 0.09 \text{ MJy sr}^{-1}$, the same numbers we find for the key project sample. In short, the typical mid-infrared emission from the outskirts of normal galaxies is reassuringly similar to what we see in the quiescent regions of the Milky Way.

We have compared galaxy mid-infrared sizes to their optical sizes, in particular those defined at the $25 \text{ } B\text{-mag arcsec}^{-2}$ level. Since this surface brightness corresponds to $0.018 \text{ MJy sr}^{-1}$ (assuming $f_B = 4260 \times 10^{-0.4m_B} \text{ Jy}$), the observed mid-infrared to B -band flux ratios at $R(0.44\mu\text{m})_{25}$ are

$$\frac{\nu I_\nu(6.75\mu\text{m})}{\nu I_\nu(0.44\mu\text{m})_{25}} \simeq 0.12 \pm 0.03 \quad \frac{\nu I_\nu(15\mu\text{m})}{\nu I_\nu(0.44\mu\text{m})_{25}} \simeq 0.15 \pm 0.04 \quad (1)$$

In other words, approximately eight (seven) times the flux is emitted at the center of the B -band as compared to the emission at $6.75 \mu\text{m}$ ($15 \mu\text{m}$), in the outskirts of normal galaxies. Once again we can contrast this with observations of Galactic cirrus. De Vaucouleurs & Pence (1978) estimated the B -band surface brightness of the Galactic disk towards the Galactic poles to be $\mu_B = 24.92 \text{ mag arcsec}^{-2}$. Thus we infer a ratio for the Galactic cirrus

to be approximately

$$\frac{\nu I_\nu(12\mu\text{m})}{\nu I_\nu(0.44\mu\text{m})_{\text{Gal. cirrus}}} \simeq 0.15, \quad (2)$$

comparable to our results at 6.75 and 15 μm .

Alternatively, it may be more illuminating to compare for quiescent regions the integrated total-infrared flux to the integrated flux in the B -band. From this comparison we can infer the ratio of heating output to heating input (i.e. the total-infrared flux to the UV and optical energy responsible for the dust heating). As a start, we contrast the integrated flux within the LW2 and LW3 bands to that in the B -band ($\Delta\nu/\nu \approx 0.22$):

$$\frac{\Delta\nu I_\nu(6.75) + \Delta\nu I_\nu(15)}{\Delta\nu I_\nu(0.44\mu\text{m})_{25}} \simeq 0.53 \pm 0.2. \quad (3)$$

Note that this is only valid for the outer regions of normal star-forming galaxies. To infer the total-infrared emission for diffuse cirrus regions using only the flux in the LW2 and LW3 bands, we have to rely on a model for the infrared spectral energy distribution of galaxies. Dale et al. (2000) present such a model for normal star-forming galaxies. Constrained by IRAS, ISO-CAM, and ISO-PHOT observations for our sample of 69 normal galaxies, the model reproduces well the empirical spectra and infrared color trends. It also allows us to determine the infrared energy budget for normal galaxies, and of particular interest here, to translate mid-infrared fluxes into total-infrared fluxes. The model shows that, for cirrus-dominated regions, the total-infrared emission (from 3–1100 μm) is approximately 10.3 times the emission appearing within just the LW2 and LW3 mid-infrared bands (and approximately 2.8 times the far-infrared emission from 42–122 μm). Coupling this result with that expressed by Equation 3, we see that

$$\frac{\text{TIR}(3 - 1100\mu\text{m})}{\Delta\nu I_\nu(0.44\mu\text{m})_{25}} \sim 5.4 \quad (4)$$

in the outskirts of normal galaxies. Observations of cirrus-dominated galaxies show that this finding is representative of quiescent disks: in our sample of normal late-type galaxies, the lowest such integrated total-infrared to blue ratios, assuming $\text{TIR}/\text{FIR} \approx 2.8$ for the most quiescent regions, are of order 3.

From the above ratio (Equation 4), one can derive the ratio of the heating output to the heating input as an indication of the optical depth in the interstellar medium. This is expected to be significantly less than unity for the most quiescent regions. All photon energies from the UV to the near-infrared contribute to the heating of dust grains. In fact, photons responsible for the B -band flux only contribute about 10-15% towards the total far-infrared flux in the outer parts of the disk of M31, a galaxy well-known for its

overall quiescent behavior (Xu & Helou 1996 and C. Xu personal communication). Thus if we assume the results from the outer disk regions of M31 can reasonably apply for the outermost portions of our normal galaxy sample, the ratio of the total heating output to the total heating input for quiescent regions is typically of order 0.7 (to within a factor of two).

7.4. The Nature of the Flux at 4.5 μm

The transition from stellar to interstellar emission is well illustrated by the spectra of Virgo Cluster galaxies collected by Boselli et al. (1998). Its precise location and therefore the interpretation to attach to mid-infrared fluxes can be parametrized by the ratio of far-infrared to visible light fluxes. Interstellar dust emission takes over by 5 μm when the FIR/B ratio exceeds 0.5, and at shorter wavelengths for higher ratios (see Table 1 for the definition of FIR/B). As might be expected, elliptical galaxies are dominated by stellar emission, both photospheric and from circumstellar dust shells, and therefore provide the templates that one subtracts to isolate the interstellar emission component in spiral galaxies (Boselli et al. 1998; Madden, Vigroux & Sauvage 1999).

We do not expect large contributions from photospheric emission at 4.5 μm for our sample in light of the results from mid-infrared ISOPHOT spectrophotometry for 45 Key Project galaxies. The shape and flux level of the 3–5 μm continuum shows no variation with the strength of the aromatic features in emission for galaxies with global far infrared to blue ratios greater than unity (and very little variation otherwise), direct evidence that this portion of the continuum arises primarily from fluctuating dust grain emission (Helou et al. 2000; Lu et al. 2000). We can similarly explore the nature of the 4.5 μm emission by analyzing the ratios of broad band fluxes. Figure 14 displays the $\frac{I_\nu(4.5\mu\text{m})}{I_\nu(6.75\mu\text{m})}$ color ratio as a function of FIR/B. Gauging by the range of observed $\frac{I_\nu(4.5\mu\text{m})}{I_\nu(6.75\mu\text{m})}$ ratios, we can immediately rule out the possibility that the emission at both 4.5 and 6.75 μm is purely photospheric: the typical logarithmic value for the early type galaxy sample of Madden, Vigroux & Sauvage (1999) is much higher ($\log \frac{I_\nu(4.5\mu\text{m})}{I_\nu(6.75\mu\text{m})} = 0.1\text{--}0.4$), consistent with the ratio for a $T = 3500$ K blackbody profile that has been suggested for the stellar component of normal galaxies (Boselli et al. 1998). Thus for our sample of normal galaxies, the average $\frac{I_\nu(4.5\mu\text{m})}{I_\nu(6.75\mu\text{m})}$ ratio tells us that the 6.75 μm emission is definitely dominated by emission from interstellar dust grains, but does not constrain the origin of the 4.5 μm emission.

The slight trend in the data can tell us more. First, the trend is in the sense of a “photospheric excess” at 4.5 μm for the galaxies with lower FIR/B. Second, the slope of this trend is consistent with the extreme scenario whereby the 4.5 μm emission is proportional to that in the B -band, while the 6.75 μm emission is directly correlated with the far-infrared

emission; the dotted line indicates the (extinction-corrected) inverse one-to-one trend. Thus, at first glance it would appear that these data suggest there are photospheric contributions to the $4.5 \mu\text{m}$ emission in normal galaxies, at least for those with $\text{FIR}/\text{B} \lesssim 1$. The small number of data points, though, limit the robustness of any such claim. Finally, if we assume that for higher FIR/B ratios ($\gtrsim 5$) the trend levels off, as the results of Helou et al. (2000) and Lu et al. (2000) suggest, then the $\frac{I_\nu(4.5\mu\text{m})}{I_\nu(6.75\mu\text{m})}$ ratio for the “pure ISM” is about 0.15.

8. Conclusion

We present mid-infrared maps at 6.75 and $15 \mu\text{m}$ for 61 normal star-forming galaxies; for a subset of 13 of these galaxies we also show maps at $4.5 \mu\text{m}$. All galaxies for which observations were attempted at these wavelengths were successfully detected. Qualitatively, the mid-infrared morphology is not a strong function of wavelength, and many of the optical features of the galaxies are also observed in the mid-infrared, except for the bulges of spiral galaxies, consistent with the findings of Helou et al. (1996) in NGC 6946. Moreover, the data support non-negligible photospheric contributions at $4.5 \mu\text{m}$ for galaxies exhibiting low FIR/B ratios, consistent with the conclusion drawn from mid-infrared ISOPHOT spectroscopy for normal galaxies (Helou et al. 2000; Lu et al. 2000). However, the evidence presented here is tenuous, as we only have broad band data at $4.5 \mu\text{m}$ for a small number of galaxies.

Mid-infrared curve of growth profiles indicate that the mid-infrared emission is very well resolved by the ISOCAM maps for most of these galaxies. Moreover, the profiles are generally exponential in nature, and the distribution of 6.75 and $15 \mu\text{m}$ emission is quite similar for most galaxies. However, four of the six galaxies that show an enhanced $\frac{I_\nu(15\mu\text{m})}{I_\nu(6.75\mu\text{m})}$ color also show signs of active central star formation, with yet greater enhancement of $\frac{I_\nu(15\mu\text{m})}{I_\nu(6.75\mu\text{m})}$ in the central regions.

Quiescent galaxies, those showing low global interstellar heating intensities (i.e. $\frac{I_\nu(60\mu\text{m})}{I_\nu(100\mu\text{m})} \geq 0.6$), have an almost constant $\frac{I_\nu(6.75\mu\text{m})}{I_\nu(15\mu\text{m})}$ color near unity. For galaxies with higher global heating intensities, the mid-infrared color drops rapidly with increasing far-infrared color. We interpret this as evidence for global mid-infrared spectral energy distributions that are increasingly dominated by H II region emission, characterized by a relatively steep slope in the mid-infrared continuum and a depressed contribution from PAHs. It is interesting to note that galaxies of all morphological types appear to follow the same color-color trend.

We have estimated the average mid-infrared surface brightness at which the mid-

infrared semi-major axis matches that in the optical (at the B -band 25 mag arcsec $^{-2}$ level). We find $R(0.44\mu\text{m})_{25} \approx R(6.75\mu\text{m})$ at 0.04 MJy sr $^{-1}$ and $R(0.44\mu\text{m})_{25} \approx R(15\mu\text{m})$ at 0.09 MJy sr $^{-1}$ on average for this sample. These mid-infrared surface brightness levels are consistent with observations of Galactic cirrus and the Solar Neighborhood, implying a reasonable similarity in interstellar heating intensity for the outskirts of normal galaxies and our Galaxy. A final interesting finding from the mid-infrared size analysis centers on the ratio of total heating output to the total heating input for quiescent regions. We find that ratio to be of order 0.7.

This work was supported by *ISO* data analysis funding from the US National Aeronautics and Space Administration, and carried out at the Infrared Processing and Analysis Center (IPAC) and the Jet Propulsion Laboratory of the California Institute of Technology. The ISOCAM data presented in this paper was analysed using CIA, a joint development by the ESA Astrophysics Division and the ISOCAM Consortium. The Digitized Sky Surveys were produced at the Space Telescope Science Institute under U.S. Government grant NAG W-2166. The images of these surveys are based on photographic data obtained using the Oschin Schmidt Telescope on Palomar Mountain and the UK Schmidt Telescope. The plates were processed into the present compressed digital form with the permission of these institutions.

REFERENCES

- Biviano, A. 1998, in *The ISOCAM Calibration Error Budget Report*
- Blommaert, J. & Cesarsky, D. 1998, in *ISOCAM Calibration Accuracies Document*
- Boselli, A., Lequeux, J., Sauvage, M., Boulade, O., Boulanger, F., Cesarsky, D., Dupraz, C., Madden, S., Viallefond, F. & Vigoux, L. 1998, A&A, 335, 53
- Boulanger, F. & Péroult, M 1998, A&A, 335, 53
- Cesarsky, C.J. et al. 1996, A&A, 315, L32
- Contursi, A., Lequeux, J., Cesarsky, D., Boulanger, F., Rubio, M., Hanus, M., Sauvage, M., Tran, D., Bosma, A., Madden, S. & Vigroux, L. 2000, A&A, submitted
- Dale, D.A., Helou, G., Silbermann, N.A., Contursi, A., Malhotra, S. & Rubin, R. 1999, AJ, 118, 2055
- Dale, D.A., Helou, G., Contursi, A., Silbermann, N.A. & Kolhatkar, S. 2000, in preparation
- de Vaucouleurs, G., de Vaucouleurs, A., Corwin, H.G., Buta, R.J., Paturel, G. & Fouqué, P. 1991. *Third Reference Catalogue of Bright Galaxies* (New York: Springer)

- de Vaucouleurs, G. & Pence, W.D. 1978, AJ, 83, 1163
- Delaney, M. 1998, in *ISOCAM Interactive Analysis User's Manual*, version 3.0
- Haynes, M., Giovanelli, R., Salzer, J.J., Wegner, G., Freudling, W., da Costa, L.N., Herter, T., Vogt, N.P. 1999, AJ, 117, 1668
- Helou, G. 1986, ApJ, 311, L33
- Helou, G., Khan, I.R., Malek, L. & Boehmer, L. 1988, ApJS, 68, 151
- Helou, G., Malhotra, S., Beichman, C.A., Dinerstein, H., Hollenbach, D.J., Hunter, D.A., Lo, K.Y., Lord, S.D., Lu, N.Y., Rubin, R.H., Stacey, G.J., Thronson, Jr., H.A. & Werner, M.W. 1996, A&A, 315, L157
- Helou, G., Becklin, E., Stencil, R.E. & Wilkes, B. 1997, *ASP Conference Series*, 124, 393
- Helou, G., Lu, N.Y., Werner, M.W., Malhotra, S. & Silbermann, N.A. 2000, ApJ Letters, in press
- Ho, L.C., Filippenko, A.V. & Sargent, W.L.W. 1995, ApJS, 98, 477
- Hunter et al. 2000, in preparation
- Kessler, M., et al. 1996, A&A, 315, L27
- Kulkarni, S. & Heiles, C. 1988, in *Galactic and Extragalactic Radio Astronomy*, eds. G.L. Verschuur & K.I. Kellermann (Springer-Verlag, New York), p. 103
- Kunze, M., Rigopoulou, D., Lutz, D. et al. 1996, A&A, 315, L101
- Lu, N.Y. et al. 2000, in preparation
- Madden, S., Vigroux, L. & Sauvage, M. 1999, in *The Universe as seen by ISO*, eds. P. Cox & M.F. Kessler (ESA SP-427, France), Vol. 2, p. 933
- Malhotra, S., Helou, G., Van Buren, D., Kong, M., Beichman, C.A., Dinerstein, H., Hollenbach, D.J., Hunter, D.A., Lo, K.Y., Lord, S.D., Lu, N.Y., Rubin, R.H., Stacey, G.J., Thronson, Jr., H.A. & Werner, M.W. 1996, A&A, 315, L161
- Reach, W.T. & Boulanger, F. 1998, in *The Local Bubble and Beyond*, eds. D. Breitschwerdt, M.J. Freyberg & J. Truemper (Springer-Verlag, Berlin)
- Ryder, S., Staveley-Smith, L., Malin, D. & Walsh, W. 1995, AJ, 109, 1592
- Schlegel, D.J., Finkbeiner, P.F. & Davis, M. 1998, ApJ, 500, 525
- Siebenmorgen, R., Starck, J.L., Sauvage, M., Cesarsky, D., Blommaert, J., Ott, S. 1997, in *ISOCAM Data User's Manual*
- Starck J.L., Abergel A., Aussel H., Sauvage, M., Gaustad, R., Claret, A., Desert, X., Delattre, C. & Pantin, E. 1999, A&AS, 134, 135

- Timmerman, R., Bertoldi, F., Wright, C.M. et al. 1996, A&A, 315, L281
- Tran, D. 1998, PhD Thesis, Univer. de Paris
- Tuffs R.J., Lemke, D., Xu, C., Davies, J.I., Gabriel, C., Heinrichsen, I., Helou, G., Hippelein, H., Lu, N.Y. & Skaley, D. 1996, A&A, 315, L149
- Valentijn, E.A., et al. 1996, A&A, 315, L145
- Vigroux, L., Charmandaris, V., Gallais, P., Laurent, O., Madden, S., Mirabel, F., Roussel, H., Sauvage, M. & Tran, D. 1999, in *The Universe as seen by ISO*, eds. P. Cox & M.F. Kessler (ESA SP-427, France), Vol. 2, p. 805
- Xu, C. & Helou, G. 1996, ApJ, 456, 163

Table 1. *ISO* Key Project Galaxies

Galaxy	R.A.(J2000) Dec h:m:s d:m:s	a ¹ '	b ¹ '	Morphology	V _⊙ km/s	Dist ² Mpc	log ₁₀ $\frac{FIR^3}{B}$
IC 10	00:20:24.5 +59:17:30	6.3	5.1	IBm?	-348	0.7	-0.48
NGC 278	00:52:04.6 +47:33:04	2.1	2.0	SAB(rs)b	640	11.8	0.01
NGC 520	01:24:35.3 +03:47:37	1.9	0.7	Irr	2266	31.6	0.36
NGC 693	01:50:31.0 +06:08:42	2.1	1.0	I0: sp	1567	22.1	0.13
NGC 695	01:51:14.2 +22:34:57	0.8	0.7	IB?(s)m: pec	9735	131.8	0.50
UGC 1449	01:58:06.7 +03:05:15	1.2	0.7	SBm pec:	5589	75.5	0.34
NGC 814	02:10:37.7 -15:46:24	1.3	0.5	SB0 ⁺ 0 ⁺ pec:	1616	21.4	0.54
NGC 986	02:33:34.1 -39:02:41	3.9	3.0	(R')SB(rs)b	2005	25.2	0.25
NGC 1022	02:38:33.0 -06:40:29	2.4	2.0	(R')SB(s)a	1453	19.4	0.26
UGC 2238	02:46:17.5 +13:05:44	1.4	1.3	Pec	6436	86.8	0.82
NGC 1155	02:58:12.9 -10:21:00	0.8	0.7	(R')SAB(s)0o: pec	4549	60.3	0.29
NGC 1156	02:59:42.6 +25:14:17	3.3	2.5	IB(s)m	375	6.4	-0.55
NGC 1222	03:08:56.8 -02:57:18	1.1	0.9	S0-pec:	2452	32.6	0.44
UGC 2519	03:09:19.9 +80:07:52	1.2	0.7	SAB?(s:)cd III:	2377	34.6	-0.04
NGC 1266	03:16:00.8 -02:25:38	1.5	1.0	(R')SB(rs)0 pec	2194	29.1	0.74
NGC 1313	03:18:15.4 -66:29:51	9.1	6.9	SB(s)d	475	3.7	-0.43
NGC 1326	03:23:56.4 -36:27:52	3.9	2.9	(R)SB(rl)0/a	1360	16.2	-0.28
NGC 1385	03:37:28.2 -24:30:04	3.4	2.0	SB(s)cd	1493	18.4	-0.03
UGC 2855	03:48:22.6 +70:07:57	4.4	2.0	SB(s)cd II-III	1202	18.7	0.31
NGC 1482	03:54:39.5 -20:30:07	2.5	1.4	SA0+ pec sp	1916	24.0	0.93
NGC 1546	04:14:37.2 -56:03:35	3.0	1.7	SA?a pec	1276	14.1	-0.22
NGC 1569	04:30:49.0 +64:50:53	3.6	1.8	IBm	-104	2.5	-0.66
NGC 2388	07:28:53.5 +33:49:05	1.0	0.6	SA(s)b: pec	4134	54.8	1.11
NGC 2366	07:28:53.7 +69:12:54	8.1	3.3	IB(s)m	100	2.9	-0.83
ESO 317- G 023	10:24:42.5 -39:18:21	1.9	0.8	(R')SB(rs)a	2892	34.7	0.53
IRAS F10565+2448	10:59:18.1 +24:32:34	0.4	0.3	Pec	12921	171.4	1.36
NGC 3583	11:14:10.8 +48:19:03	2.8	1.8	SB(s)b	2136	29.2	-0.18
NGC 3620	11:16:04.3 -76:12:54	2.8	1.1	(R')SB(s)ab	1680	19.0
NGC 3683	11:27:32.0 +56:52:43	1.9	0.7	SB(s)c?	1716	24.2	0.42
NGC 3705	11:30:06.7 +09:16:36	4.9	2.0	SAB(r)ab	1018	11.9	-0.62
NGC 3885	11:46:46.5 -27:55:22	2.4	1.0	SAB(r:)0/a:	1802	20.8	0.04
NGC 3949	11:53:41.4 +47:51:32	2.9	1.7	SA(s)bc:	807	11.6	-0.19
NGC 4102	12:06:23.1 +52:42:39	3.0	1.7	SAB(s)b?	837	12.4	0.54
NGC 4194	12:11:09.6 +54:31:35	1.8	1.1	IBm pec	2506	34.8	0.63
NGC 4418	12:26:54.6 -00:52:40	1.4	0.7	(R')SAB(s)a	2179	27.3	1.15
NGC 4490	12:30:36.9 +41:38:23	6.3	3.1	SB(s)d pec	565	8.2	-0.20

Table 1—Continued

Galaxy	R.A.(J2000) h:m:s	Dec d:m:s	a ¹ '	b ¹ '	Morphology	V _⊙ km/s	Dist ² Mpc	log ₁₀ $\frac{\text{FIR}^3}{B}$
NGC 4519	12:33:30.3	+08:39:17	3.2	2.5	SB(rs)d	1220	15.1	-0.30
NGC 4713	12:49:57.8	+05:18:39	2.7	1.7	SAB(rs)d	652	7.4	-0.30
IC 3908	12:56:40.4	-07:33:40	1.8	0.7	SB(s)d?	1296	15.4	0.29
IC 860	13:15:03.5	+24:37:08	0.5	0.3	SB(s)a:	3347	44.7	1.04
IC 883	13:20:35.3	+34:08:22	1.5	1.1	Pec	7000	94.0	1.14
NGC 5433	14:02:36.0	+32:30:38	1.6	0.4	SAB(s)c:	4354	59.0	0.33
NGC 5713	14:40:11.3	-00:17:27	2.8	2.5	SAB(rs)bc pec	1883	24.7	0.20
NGC 5786	14:58:56.7	-42:00:45	2.3	1.1	(R')SAB(s)bc	2998	37.9	-0.49
NGC 5866	15:06:29.4	+55:45:49	4.7	1.9	S0	672	11.4	-0.61
CGCG 1510.8+0725	15:13:13.3	+07:13:27	0.4	0.2	SB?(s?)0/a pec	3897	52.4	1.43
NGC 5962	15:36:31.7	+16:36:32	3.0	2.1	SA(r)c	1958	27.3	-0.09
IC 4595	16:20:44.2	-70:08:35	2.7	0.5	SB?c sp II:	3410	42.9	0.14
NGC 6286	16:58:31.4	+58:56:13	1.3	1.2	SB(s)0+ pec?	5501	76.5	0.83
IC 4662	17:47:06.4	-64:38:25	2.8	1.6	IBm	308	2.1	-0.38
NGC 6753	19:11:23.3	-57:02:56	2.5	2.1	(R)SA(r)b	3124	40.4	-0.02
NGC 6821	19:44:24.1	-06:50:02	1.2	1.0	SB(s)d:	1525	22.5	-0.17
NGC 6822	19:44:56.1	-14:48:05	15.5	13.5	IB(s)m	-57	0.7	-0.58
NGC 6946	20:34:52.3	+60:09:14	11.5	9.8	SAB(rs)cd	48	5.5	-0.34
NGC 6958	20:48:42.2	-37:59:42	2.1	1.7	E+	2713	36.4	-0.88
NGC 7218	22:10:11.7	-16:39:36	2.5	1.1	SB(r)c	1662	23.8	-0.17
NGC 7418	22:56:36.0	-37:01:47	3.5	2.6	SAB(rs)cd	1446	19.4	-0.33
IC 5325	23:28:43.1	-41:19:58	2.8	2.5	SAB(rs)bc	1503	19.7	-0.26
IRAS F23365+3604	23:39:01.3	+36:21:10	0.5	0.3	S?Ba? pec or Pec	19331	261.2	1.16
NGC 7771	23:51:24.8	+20:06:42	2.5	1.0	SB(s)a	4277	60.0	0.41
Markarian 331	23:51:26.8	+20:35:10	0.7	0.4	SA(s)a: pec	5541	76.8	1.12

¹The RC3 major and minor diameters at the B -band 25 mag arcsec⁻² level (de Vaucouleurs et al. 1991).

²Distances computed in the Local Group reference frame assuming a Hubble constant of 75 km s⁻¹ Mpc⁻¹.

³FIR is defined as in Helou et al. (1988): $1.26 \cdot 10^{-11} (2.58 I_\nu(60\mu\text{m}) + I_\nu(100\mu\text{m})) \text{ W m}^{-2}$ where the IRAS flux densities are in units of Jy (see Table 4). The monochromatic B-band flux is computed from $\nu I_\nu(0.44\mu\text{m})$ where $I_\nu = 4260 \cdot 10^{-0.4m_B} \text{ Jy}$ and m_B is the k -corrected face-on B-band apparent magnitude corrected for Galactic extinction (Schlegel, Finkbeiner & Davis 1998). We have adopted the RC3 k and internal extinction corrections.

Table 2. CAM Observations- 2×2 Raster Maps

Galaxy	Date	Rev ¹	Integration (sec)	
			15 μ m	6.75 μ m
NGC 278	05 Jul 1997	597	157	151
NGC 520	01 Jan 1998	777 ²	157	151
NGC 693	03 Jul 1997	595	157	151
NGC 695	10 Aug 1997	633	157	151
UGC 1449	24 Jun 1997	586	157	151
NGC 814	06 Jul 1997	598	157	151
NGC 986	27 Nov 1997	743	157	151
NGC 1022	08 Jan 1998	784	157	151
UGC 2238	10 Aug 1997	633	157	151
NGC 1155	13 Jul 1997	605	157	151
NGC 1156	29 Aug 1997	653	157	151
NGC 1222 ³	16 Feb 1998	824	151
UGC 2519	16 Oct 1997	701	157	151
NGC 1266	12 Jan 1998	788	157	151
NGC 1326	04 Dec 1997	750 ²	157	151
NGC 1385	19 Jan 1998	796	157	151
UGC 2855	06 Aug 1997	629	157	151
NGC 1482	19 Jan 1998	796 ²	157	151
NGC 1546	04 Oct 1997	689	157	151
NGC 1569	27 Mar 1998	863 ⁴	157	151
NGC 2388	03 Nov 1997	718 ²	157	151
ESO 317- G 023	25 Jul 1996	252	63	121
IRAS F10565+2448	05 Jun 1996	202	63	121
NGC 3583	30 May 1996	195	63	121
NGC 3620	18 Aug 1996	276	63	121
NGC 3620	21 Sep 1997	675 ²
NGC 3683	29 May 1996	194	63	121
NGC 3705	19 May 1996	184	63	121
NGC 3885	26 Jul 1996	252	63	121
NGC 3949	30 May 1996	195	63	121
NGC 4102	30 May 1996	195	63	121
NGC 4194	29 May 1996	194	63	121
NGC 4418	14 Jul 1996	241	63	121
NGC 4490	09 Jun 1996	205	63	121
NGC 4519	10 Jul 1996	236	63	121
NGC 4713	29 Jun 1996	225	63	121

Table 2—Continued

Galaxy	Date	Rev ¹	Integration (sec)	
			15 μm	6.75 μm
IC 3908	26 Jul 1996	252	63	121
IC 860	16 Jul 1996	243	63	121
IC 883	19 Jun 1996	215	63	121
NGC 5433	09 Jun 1997	571	157	151
NGC 5713	26 Aug 1996	284	63	121
NGC 5713	05 Aug 1997	628 ²
NGC 5786	10 Sep 1996	299	63	121
NGC 5866	08 Aug 1997	631 ²
CGCG 1510.8+0725	24 Aug 1996	281	63	121
NGC 5962	20 Aug 1996	278	63	121
IC 4595	19 Aug 1996	276	63	121
IC 4595	03 Aug 1997	626 ²
NGC 6286	11 Jun 1996	207	63	121
IC 4662	25 Aug 1997	648	63	121
NGC 6753	10 Sep 1996	299	63	121
NGC 6753	31 Oct 1997	716 ²
NGC 6821	30 Sep 1996	319	63	121
NGC 6958	11 May 1997	542	157	151
NGC 7218	19 Nov 1996	369	63	121
NGC 7418	19 Nov 1996	369	63	121
IC 5325	20 Nov 1996	369	63	121
IRAS F23365+3604	07 Dec 1997	752	157	151
NGC 7771	03 Jun 1997	565	63	121
NGC 7771	01 Dec 1997	747 ²
Markarian 331	03 Jun 1997	565	63	121

¹Revolution number (orbit) in which the data were obtained

²A 4.5 μm map was obtained during this revolution. The integration time was 302 seconds for a 4.5 μm map.

³The 15 μm observation for NGC 1222 failed.

⁴NGC 1569 was observed using several of the ISOCAM filters. More details are given in the text and in Table 6.

Table 3. CAM Observations-Large Maps

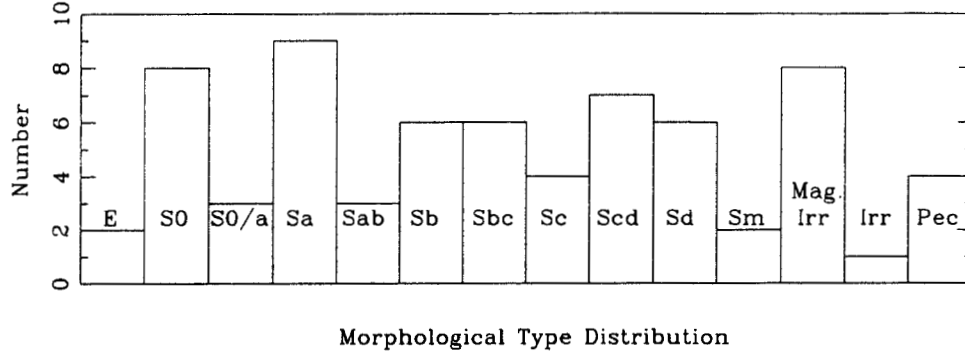
Galaxy	Date	Rev ¹	Integration (seconds)			rastering	Size
			15 μm	6.75 μm	4.5 μm		
IC 10	15 Feb 1997	457	504	605	4 \times 4	7'25 \times 7'25
IC 10 ²	16 Feb 1998	841	630	605	1210	4 \times 4	7'25 \times 7'25
NGC 1313	18 Apr 1997	519	1008	1210	2 \times 4 \times 4	11'85 \times 9'20
NGC 1313	08 Sep 1997	663	2419	2 \times 4 \times 4	9'20 \times 11'85
NGC 2366	04 Sep 1997	658	840	1008	5 \times 5	8'20 \times 8'20
NGC 6822	03 Nov 1997	719	2352	2822	8 \times 8	12'65 \times 12'65
NGC 6946	08 Feb 1996	83	1176	2258	8 \times 8	12'65 \times 12'65

¹Revolution number (orbit) in which the data were obtained.

²IC 10 was also observed at 11.4 μm during this revolution for 605 seconds.

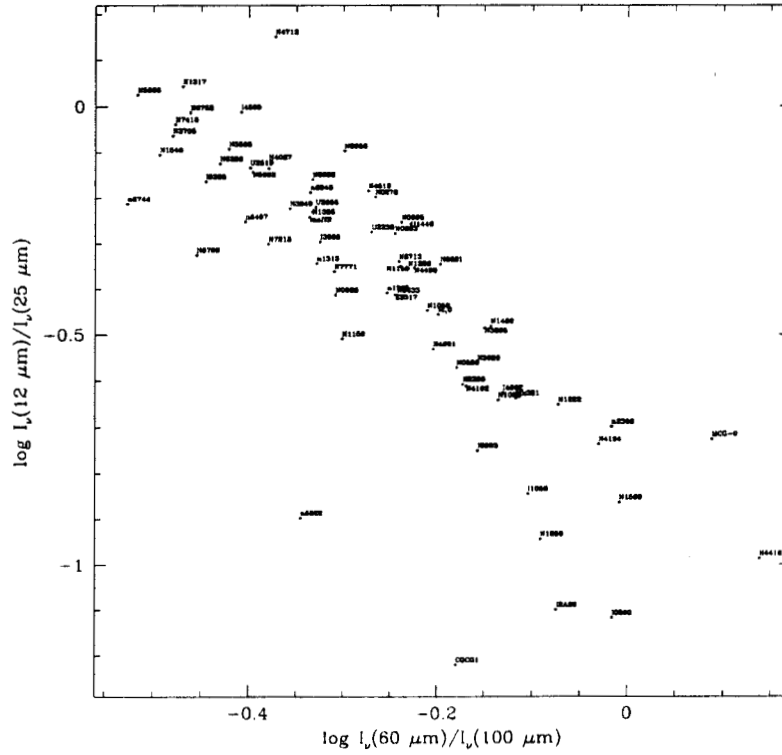
Table 4. Flux Densities

Galaxy	12 μm Jy	25 μm Jy	60 μm Jy	100 μm Jy	6.75 μm Jy	15 μm Jy
IC 10	4.88	13.95	112.92	178.56	2.18 \pm 0.44	3.06 \pm 0.61
NGC 278	1.63	2.57	25.05	46.22	1.12 \pm 0.23	1.18 \pm 0.24
NGC 520	0.76	2.84	31.10	46.99	0.52 \pm 0.13:	0.86 \pm 0.18
NGC 693	0.29	0.55	6.73	11.83	0.18 \pm 0.04	0.18 \pm 0.05
NGC 695	0.48	0.86	7.87	13.62	0.25 \pm 0.05	0.36 \pm 0.09
UGC 1449	0.31	0.56	4.96	8.39	0.18 \pm 0.04	0.17 \pm 0.03
NGC 814	0.19	1.01	4.41	3.60	0.05 \pm 0.01	0.22 \pm 0.05
NGC 986	1.41	3.65	25.14	51.11	0.51 \pm 0.13:	1.07 \pm 0.25
NGC 1022	0.75	3.29	19.83	27.09	0.31 \pm 0.08:	0.77 \pm 0.16
UGC 2238	0.34	0.53	8.40	0.54	0.24 \pm 0.05	0.30 \pm 0.07
NGC 1155	0.21	0.47	2.89	5.01	0.05 \pm 0.01	0.09 \pm 0.02
NGC 1156	0.17	0.55	5.24	10.48	0.09 \pm 0.02	0.14 \pm 0.03
NGC 1222	0.51	2.29	13.07	15.45	0.27 \pm 0.06
UGC 2519	0.25	0.34	2.98	7.46	0.12 \pm 0.03	0.17 \pm 0.04
NGC 1266	0.14	1.23	13.32	16.43	0.04 \pm 0.01	0.15 \pm 0.03
NGC 1313	1.70	3.75	45.69	97.25	0.69 \pm 0.14	0.84 \pm 0.17
NGC 1326	0.38	0.86	8.17	13.90	0.18 \pm 0.04	0.32 \pm 0.07
NGC 1385	1.19	2.02	17.30	37.23	0.72 \pm 0.15	0.76 \pm 0.16
UGC 2855 ²	2.93	4.86	42.39	90.49	>2.15 \pm 0.54	>2.39 \pm 0.60
NGC 1482	1.54	4.67	33.45	46.53	0.78 \pm 0.20:	1.37 \pm 0.28
NGC 1546	0.62	0.79	7.21	22.44	0.42 \pm 0.08	0.56 \pm 0.12
NGC 1569	1.23	8.98	54.25	55.30	0.32 \pm 0.06	1.43 \pm 0.29
NGC 2388	0.51	2.07	17.01	25.33	0.23 \pm 0.05	0.50 \pm 0.11
NGC 2366	0.21	1.05	4.85	5.04	0.02 \pm 0.005	0.17 \pm 0.04
ESO 317-G 023	0.34	0.88	13.50	23.71	0.18 \pm 0.04	0.27 \pm 0.06
IRAS F10565+2448	0.17	1.19	12.08	15.36	0.09 \pm 0.02	0.27 \pm 0.08
NGC 3583	0.63	0.78	7.08	18.66	0.29 \pm 0.06	0.41 \pm 0.08
NGC 3620	1.29	4.71	46.80	67.26	0.63 \pm 0.16:	1.06 \pm 0.22
NGC 3683	1.06	1.53	13.61	29.27	0.64 \pm 0.13	0.76 \pm 0.16
NGC 3705	0.38	0.44	3.72	11.22	0.19 \pm 0.05	0.27 \pm 0.09
NGC 3885	0.46	1.41	11.66	16.46	0.33 \pm 0.08:	0.45 \pm 0.10
NGC 3949	0.82	1.37	11.28	26.65	0.42 \pm 0.09	0.50 \pm 0.12
NGC 4102	1.72	7.05	48.10	71.01	0.66 \pm 0.16:	1.61 \pm 0.40:
NGC 4194	0.83	4.53	23.72	25.44	0.41 \pm 0.10:	0.84 \pm 0.17
NGC 4418	1.00	9.69	43.89	31.94	0.24 \pm 0.06:	1.56 \pm 0.39:
NGC 4490 ²	1.86	4.20	45.90	76.93	>1.07 \pm 0.27	>1.40 \pm 0.35



Nov 12 08:21:12 1999

Fig. 1.— Histogram of morphological types for the 61 galaxies in our sample.



Nov 12 08:21:56 1999

Fig. 2.— *IRAS* color-color diagram for the 61 galaxies in the U.S. Key Project on normal galaxies ISOCAM sample.

Table 4—Continued

Galaxy	12 μ m Jy	25 μ m Jy	60 μ m Jy	100 μ m Jy	6.75 μ m Jy	15 μ m Jy
NGC 4519	0.36	0.55	3.74	7.02	0.11 \pm 0.02	0.23 \pm 0.05
NGC 4713	0.24	0.17	4.60	10.84	0.15 \pm 0.03	0.21 \pm 0.05
IC 3908	0.44	0.87	8.09	17.08	0.44 \pm 0.10	0.43 \pm 0.12
IC 860	0.10	1.31	17.93	18.60	0.02 \pm 0.004	0.06 \pm 0.02
IC 883	0.25	1.41	17.01	24.41	0.16 \pm 0.03	0.25 \pm 0.05
NGC 5433	0.27	0.70	6.62	11.57	0.18 \pm 0.04	0.30 \pm 0.07
NGC 5713	1.30	2.84	21.89	38.09	0.88 \pm 0.18	1.06 \pm 0.22
NGC 5786	0.36	0.76	5.26	14.98	0.30 \pm 0.07	0.39 \pm 0.11
NGC 5866	0.36	0.34	5.21	17.11
CGCG1510.8+0725	0.05	0.83	20.84	31.52	0.04 \pm 0.01	0.08 \pm 0.03
NGC 5962	0.74	1.03	8.89	22.11	0.37 \pm 0.08	0.51 \pm 0.12
IC 4595	0.71	0.73	7.05	18.04	0.30 \pm 0.07	0.39 \pm 0.12
NGC 6286	0.42	0.56	8.22	22.13	0.17 \pm 0.03	0.20 \pm 0.04
IC 4662	0.30	1.27	8.81	11.90	0.05 \pm 0.02	0.17 \pm 0.04
NGC 6753	0.95	0.98	9.77	28.26	0.38 \pm 0.08	0.51 \pm 0.12
NGC 6821	0.14	0.31	3.63	5.71	0.06 \pm 0.01	0.13 \pm 0.04
NGC 6822	0.84	6.63	58.86	130.32	0.10 \pm 0.02	0.31 \pm 0.06
NGC 6946	15.17	23.34	167.72	362.66	11.19 \pm 2.24	11.49 \pm 2.30
NGC 6958	0.16	0.20	1.00	1.99	0.03 \pm 0.01	0.03 \pm 0.01
NGC 7218	0.28	0.56	4.67	11.18	0.21 \pm 0.04	0.28 \pm 0.07
NGC 7418	0.63	0.69	5.38	16.13	0.23 \pm 0.05	0.29 \pm 0.07
IC 5325	0.48	0.70	5.15	14.35	0.24 \pm 0.06	0.31 \pm 0.08
IRAS 23365+3604	0.13	0.88	7.44	8.83	0.02 \pm 0.005	0.11 \pm 0.02
NGC 7771	0.77	1.77	19.67	40.12	0.46 \pm 0.11:	0.59 \pm 0.12
Mark 0331	0.55	2.39	18.04	23.61	0.21 \pm 0.05:	0.52 \pm 0.11

¹Fluxes with a colon indicate ADC saturation problems. These flux densities are lower limits.

²We estimate the total uncertainty in the flux density measures for NGC 4490 and UGC 2855 to be somewhat larger than the sample average uncertainty, since these galaxies are large compared to our mid-infrared maps.

Table 5. 4.5 μm Fluxes

Galaxy	Flux Jy
IC 10	0.45 ± 0.11
NGC 520	0.07 ± 0.02
NGC 1313	0.10 ± 0.03
NGC 1326	0.09 ± 0.02
NGC 1482	0.10 ± 0.02
NGC 1569	0.11 ± 0.03
NGC 2388	0.03 ± 0.01
NGC 3620	0.14 ± 0.03
NGC 5713	0.10 ± 0.03
NGC 5866	0.22 ± 0.05
IC 4595	0.05 ± 0.02
NGC 6753	0.14 ± 0.03
NGC 7771	0.12 ± 0.03

Table 6. NGC 1569 Fluxes

Filter	λ μm	Flux Jy
LW1	4.5	0.11 ± 0.03
LW4	6.0	0.15 ± 0.03
LW2	6.7	0.32 ± 0.06
LW6	7.7	0.40 ± 0.08
LW7	9.6	0.44 ± 0.09
LW8	11.3	0.78 ± 0.16
LW3	15.0	1.43 ± 0.29
LW9	14.9	1.82 ± 0.36

Fig. 3.— Optical (from the Digitized Sky Survey) and mid-infrared maps for the ISOCAM sample. The first frame is from the DSS. The second frame, if available, is the $4.5\ \mu\text{m}$ map, and the third and fourth frames are the 6.75 and $15\ \mu\text{m}$ maps. The coordinate system included in the DSS frame indicates the N-E orientation for the DSS, 6.75 and $15\ \mu\text{m}$ frames, with the arrow pointing towards N. The $4.5\ \mu\text{m}$ observations were done at a different roll angle, so we have also included the N-E orientation for those observations.

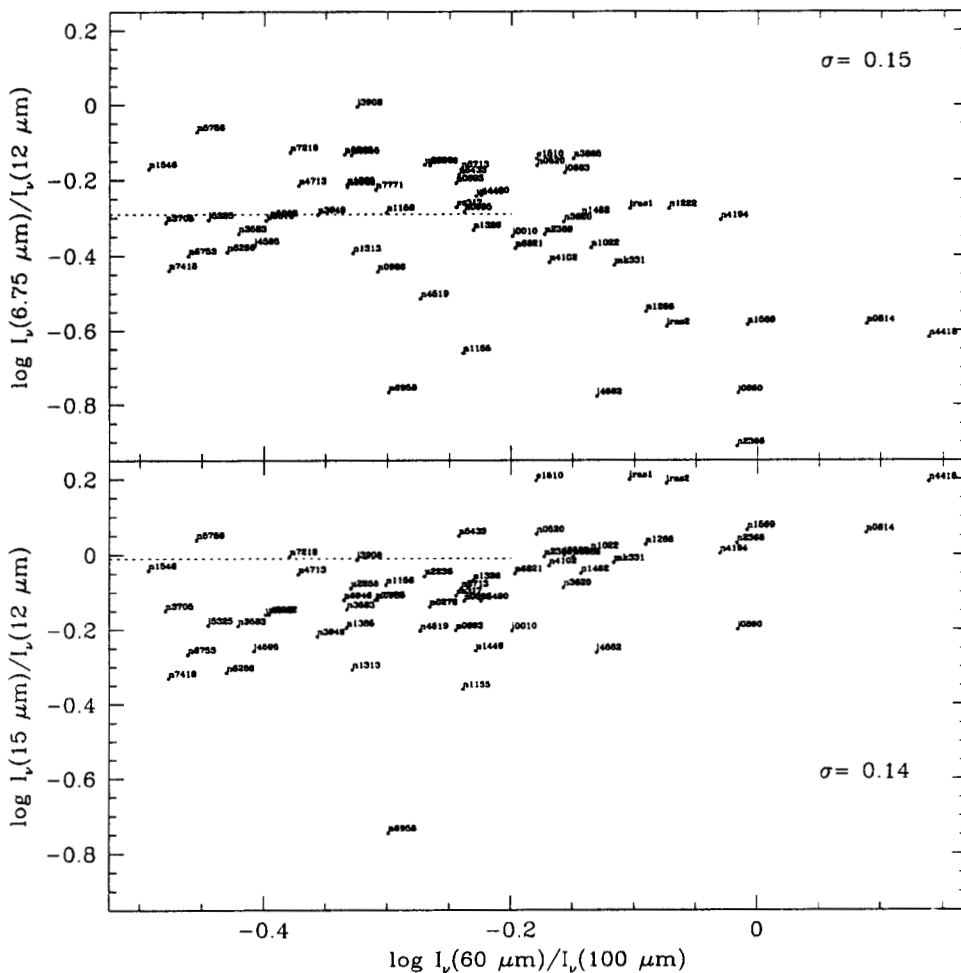
Fig. 4.— Digitized Sky Survey optical and ISOCAM mid-infrared maps at 4.5 , 6.75 , 11.4 , and $15\ \mu\text{m}$ of IC 10. The coordinate system included in the DSS frame indicates the N-E orientation, with the arrow pointing towards N.

Fig. 5.— Digitized Sky Survey optical and ISOCAM mid-infrared maps at 4.5 , 6.75 , and $15\ \mu\text{m}$ of NGC 1313. The coordinate system included in the DSS frame indicates the N-E orientation, with the arrow pointing towards N. The roll angle for the $4.5\ \mu\text{m}$ observations were done at a different roll angle, so we have rotated the image for N-E orientation consistency.

Fig. 6.— Digitized Sky Survey optical and ISOCAM mid-infrared maps at 6.75 and $15\ \mu\text{m}$ of NGC 2366. The coordinate system included in the DSS frame indicates the N-E orientation, with the arrow pointing towards N.

Fig. 7.— Digitized Sky Survey optical and ISOCAM mid-infrared maps at 6.75 and $15\ \mu\text{m}$ of NGC 6822. The coordinate system included in the DSS frame indicates the N-E orientation, with the arrow pointing towards N.

Fig. 8.— Digitized Sky Survey optical and ISOCAM mid-infrared maps at 6.75 and $15\ \mu\text{m}$ of NGC 6946. The coordinate system included in the DSS frame indicates the N-E orientation, with the arrow pointing towards N.



Nov 12 09:16:50 1999

Fig. 9.— Color-color diagrams showing the comparison of *ISO* fluxes to *IRAS* 12 μ m fluxes. The dashed lines indicate the $\frac{I_{\nu}(6.75\mu\text{m})}{I_{\nu}(12\mu\text{m})}$ and $\frac{I_{\nu}(15\mu\text{m})}{I_{\nu}(12\mu\text{m})}$ values for a cirrus model (Reach 1999). The σ values are the standard deviations in the ordinates between $-0.5 < \log \frac{I_{\nu}(60\mu\text{m})}{I_{\nu}(100\mu\text{m})} < -0.2$.

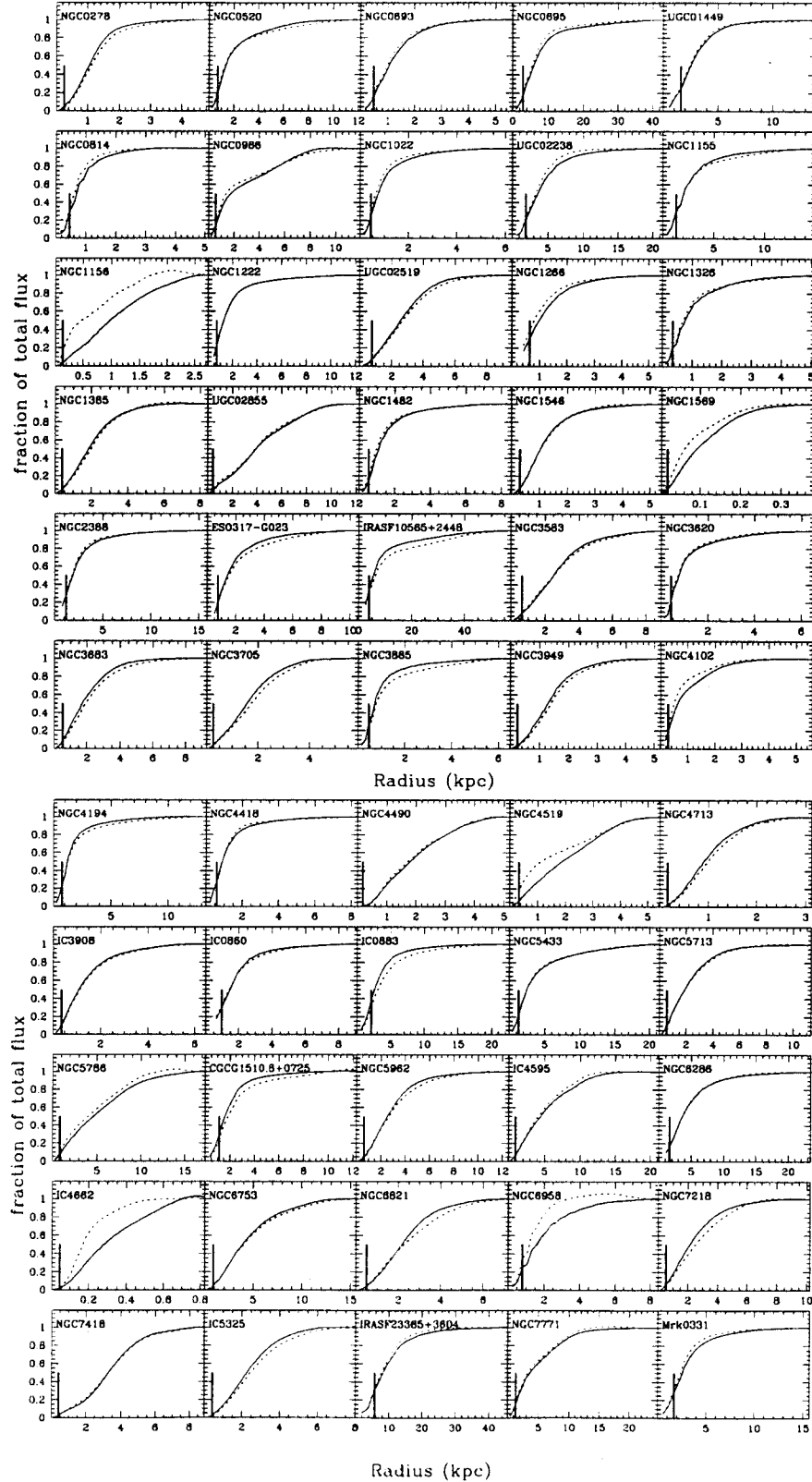
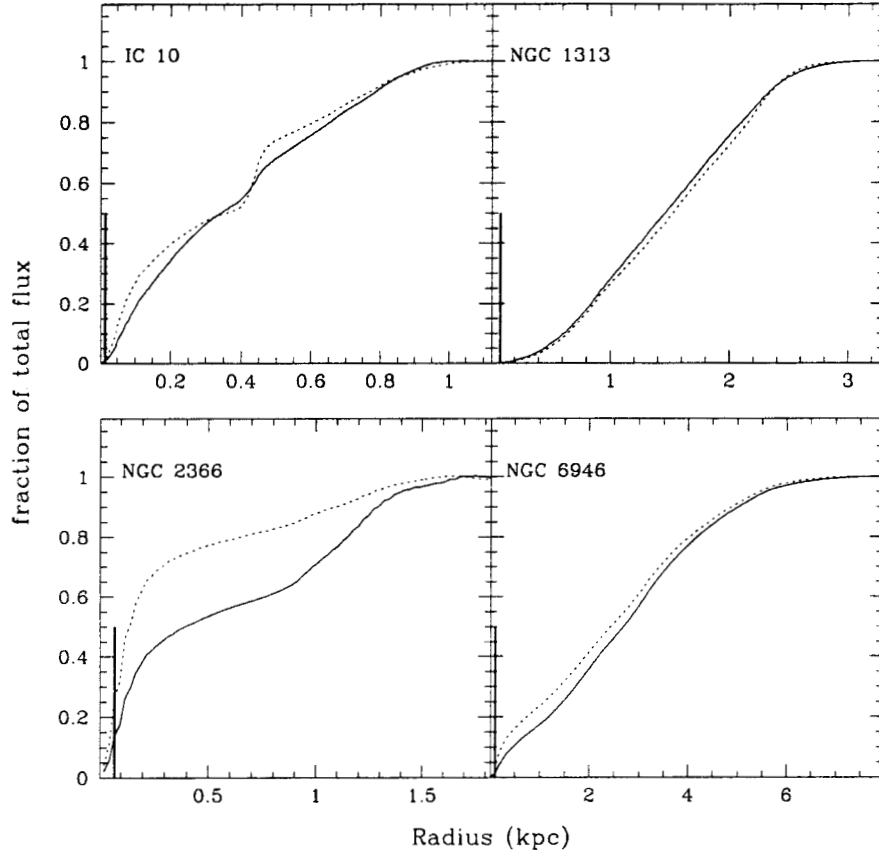
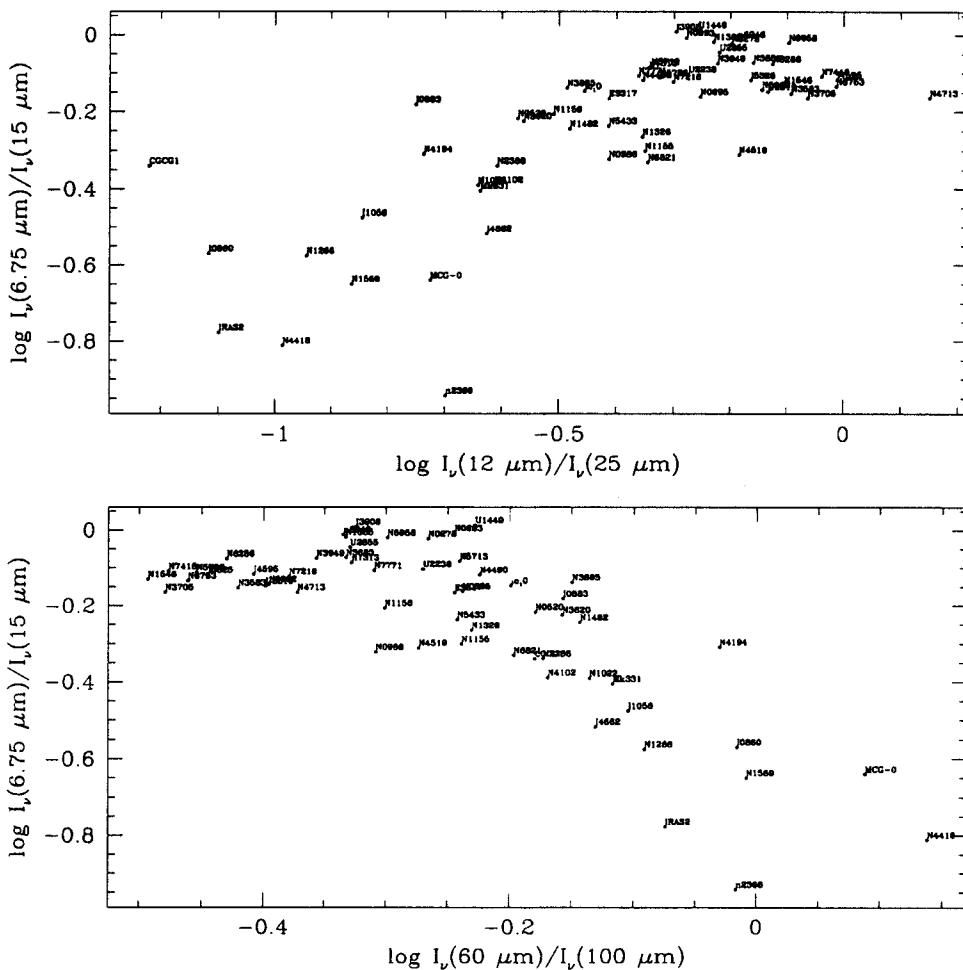


Fig. 10.— Mid-infrared flux curve of growth profiles for the galaxies with 2×2 raster maps.



Dec 15 11:01:48 1999

Fig. 11.— Mid-infrared flux curve of growth profiles for the galaxies with relatively large raster maps. The solid line is the growth profile for 6.75 μm . The dashed line is the growth profile for 15 μm . The short bold solid line on the abscissa indicates the 4.5'' HWHW resolution limit for our images.



Nov 12 09:19:25 1999

Fig. 12.— Mid-infrared versus far-infrared color-color diagrams. For a range of moderate heating intensity levels, $-0.5 < \log \frac{I_\nu(60\mu\text{m})}{I_\nu(100\mu\text{m})} < -0.2$, normal galaxies have a similar mid-infrared color.

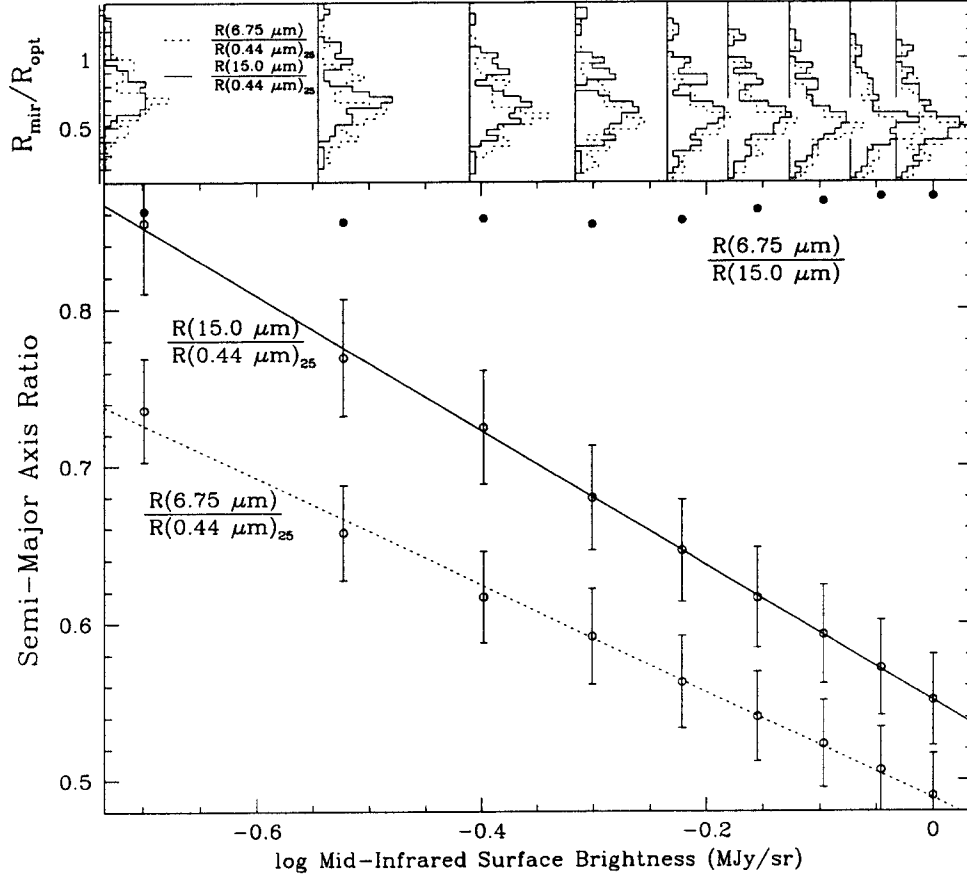
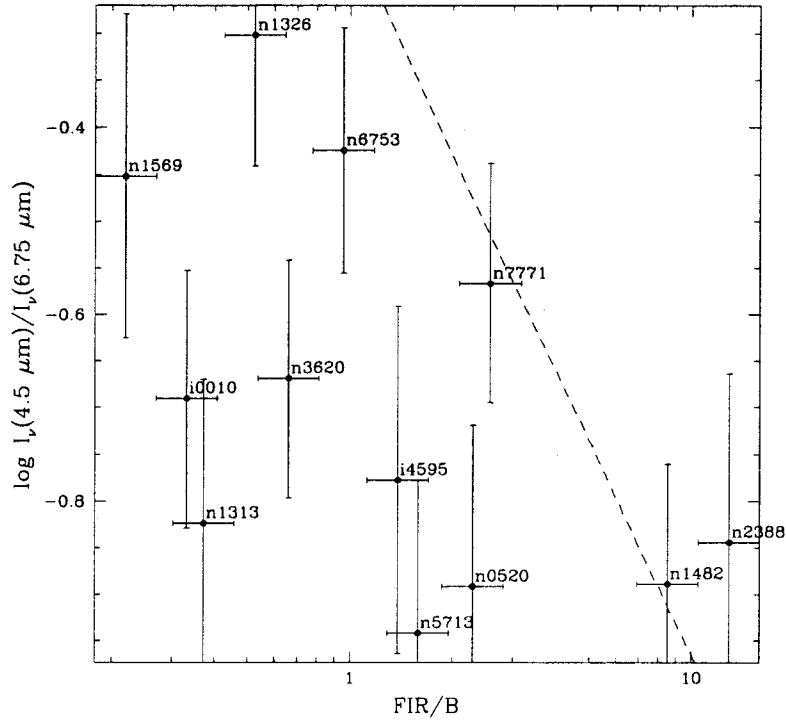


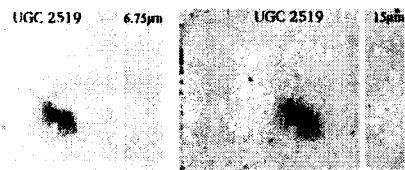
Fig. 13.— The size of the mid-infrared semi-major axis, normalized to the B -band 25 mag arcsec⁻² semi-major axis $R(0.44\mu\text{m})_{25}$, as a function of the infrared surface brightness level. The mid-infrared size at $6.75 \mu\text{m}$ ($15 \mu\text{m}$) matches $R(0.44\mu\text{m})_{25}$ at a surface brightness level of 0.04 MJy sr^{-1} (0.09 MJy sr^{-1}). The histograms at the top of the diagram indicate the distributions of size ratios at each mid-infrared surface brightness level. The filled circles show the running ratio of the 6.75 to $15 \mu\text{m}$ sizes.



Feb 14 12:24:35 2000

Fig. 14.— A comparison of the 4.5 to 6.75 μm emission as a function of the far infrared to blue ratio. A slight trend is seen in the expected sense (see text), whereby galaxies with a higher FIR/B exhibit comparatively more 4.5 μm emission. The expected 4.5 to 6.75 μm logarithmic ratio for photospheric emission (assuming a $T \sim 3500$ K blackbody; see Boselli et al. 1998) is 0.28, consistent with the findings of Madden, Vigroux & Sauvage (1999) for early type galaxies.

UGC 2519 DSS



NGC 1266 DSS



NGC 1326 DSS

NGC 1326 4.5µm



NGC 1385 DSS



UGC 2855 DSS



NGC 1482 DSS

NGC 1482 4.5µm



NGC 1546 DSS

NGC 1546 6.75µm

NGC 1546 15µm

NGC 1569 DSS

NGC 1569 ISOCAM LW1

NGC 1569 ISOCAM LW2

NGC 1569 ISOCAM LW3

NGC 2388 DSS

NGC 2388 4.5µm

NGC 2388 6.75µm

NGC 2388 15µm

ESO 317- G 023 DSS

ESO 317 6.75µm

ESO 317 15µm

IRAS F10565 DSS

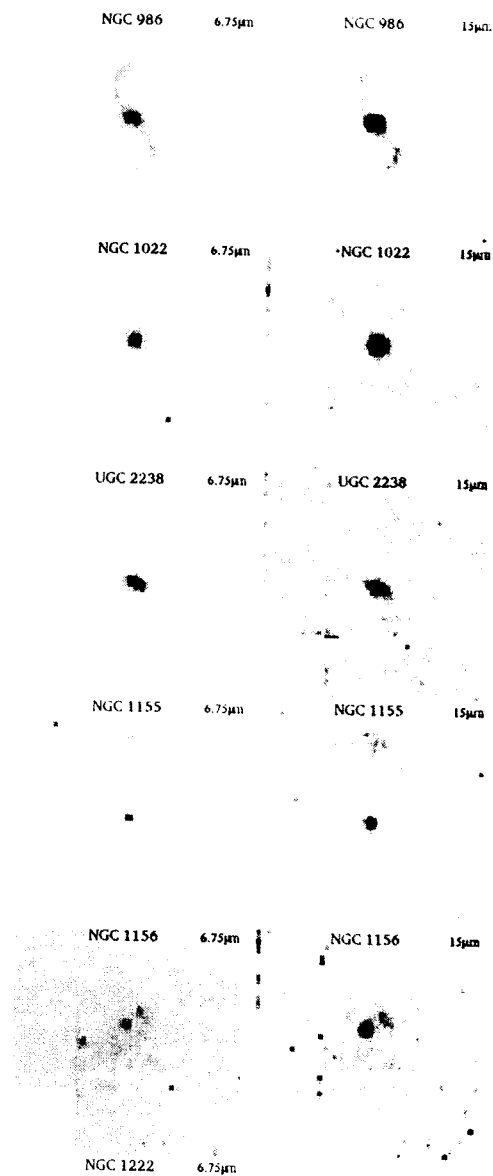
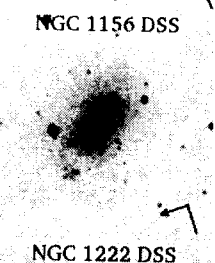
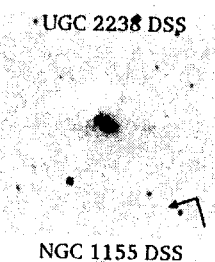
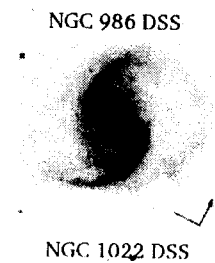
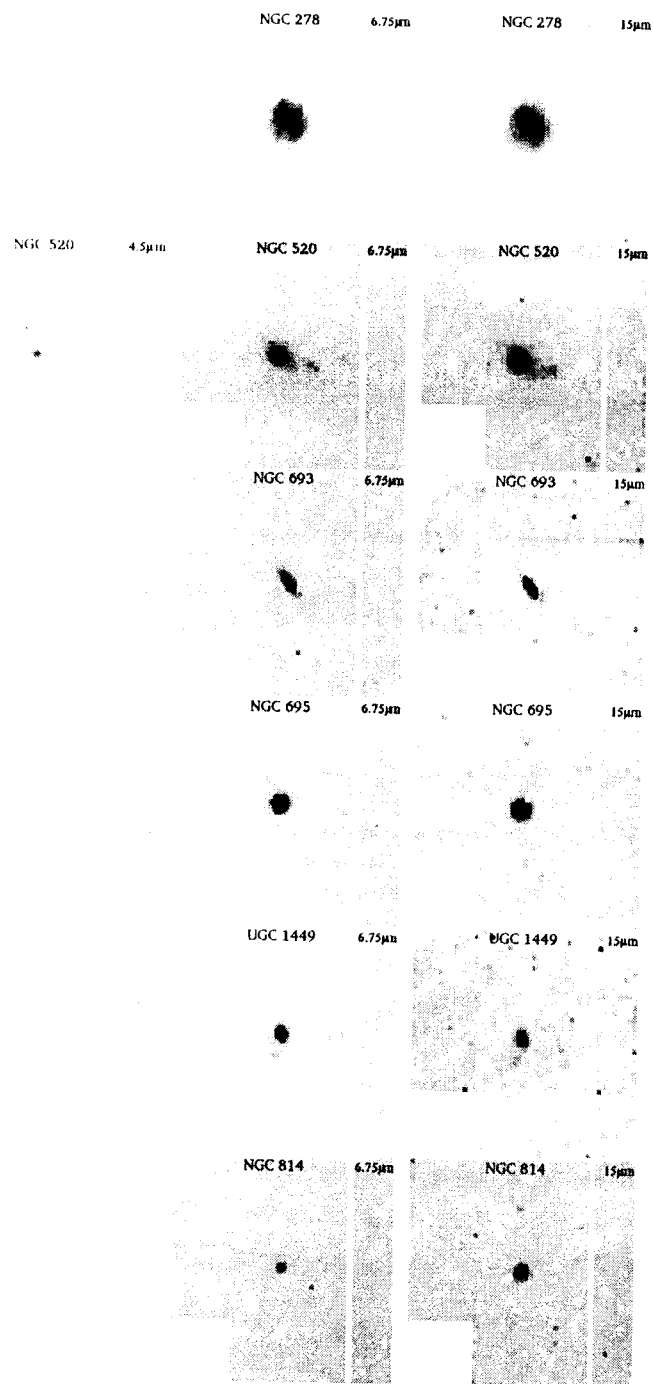
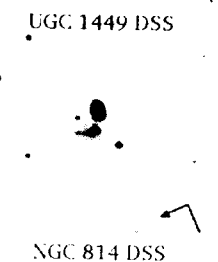
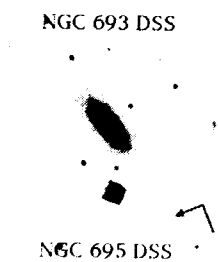
IRAS F10565 6.75µm

IRAS F10565 15µm

NGC 3583 DSS

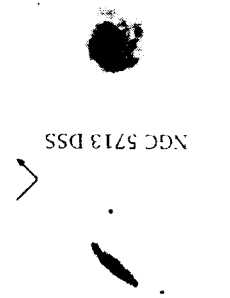
NGC 3583 6.75µm

NGC 3583 15µm





NGC 5866 DSS



NGC 5713 DSS



NGC 5433 DSS

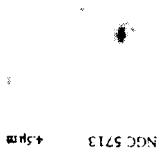


IC 883 DSS

IC 860 DSS



NGC 5866



NGC 5713



NGC 5433

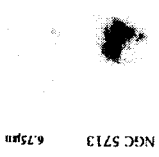


IC 883

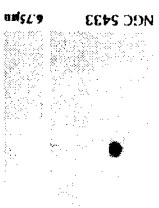
IC 860



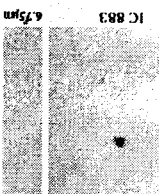
NGC 5786



NGC 5713



NGC 5433

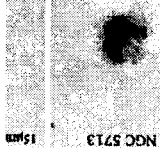


IC 883

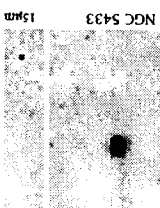
IC 860



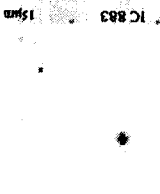
NGC 5786



NGC 5713



NGC 5433

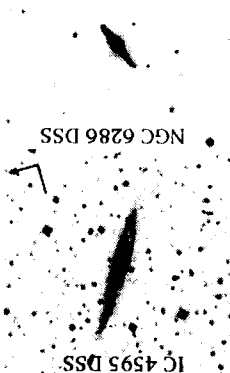


IC 883

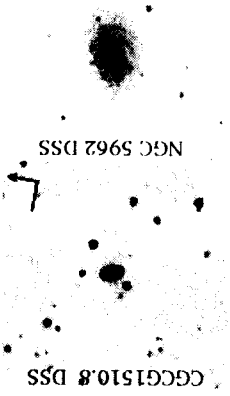
IC 860



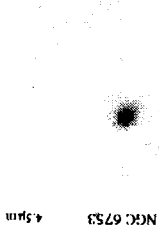
NGC 6753 DSS



IC 4595 DSS



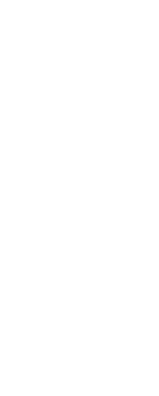
CGCG1510.8 DSS



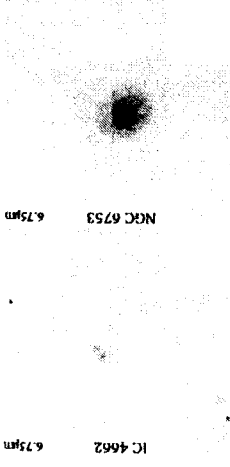
NGC 6753



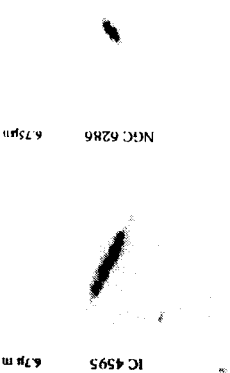
IC 4595



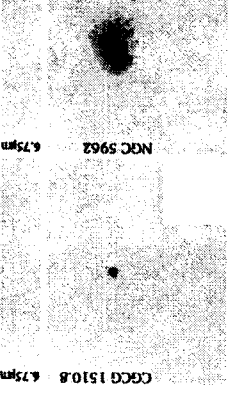
CGCG1510.8



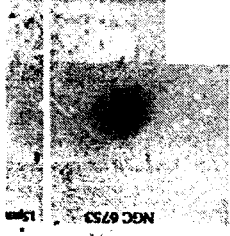
NGC 6753



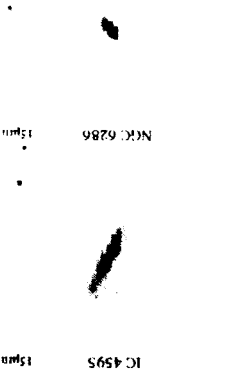
IC 4595



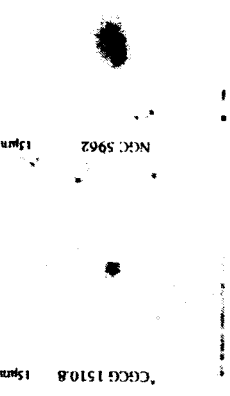
CGCG1510.8



NGC 6753

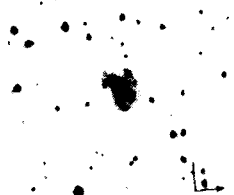


IC 4595



CGCG1510.8

NGC 6821 DSS



NGC 6958 DSS



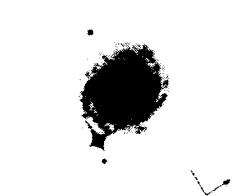
NGC 7218 DSS



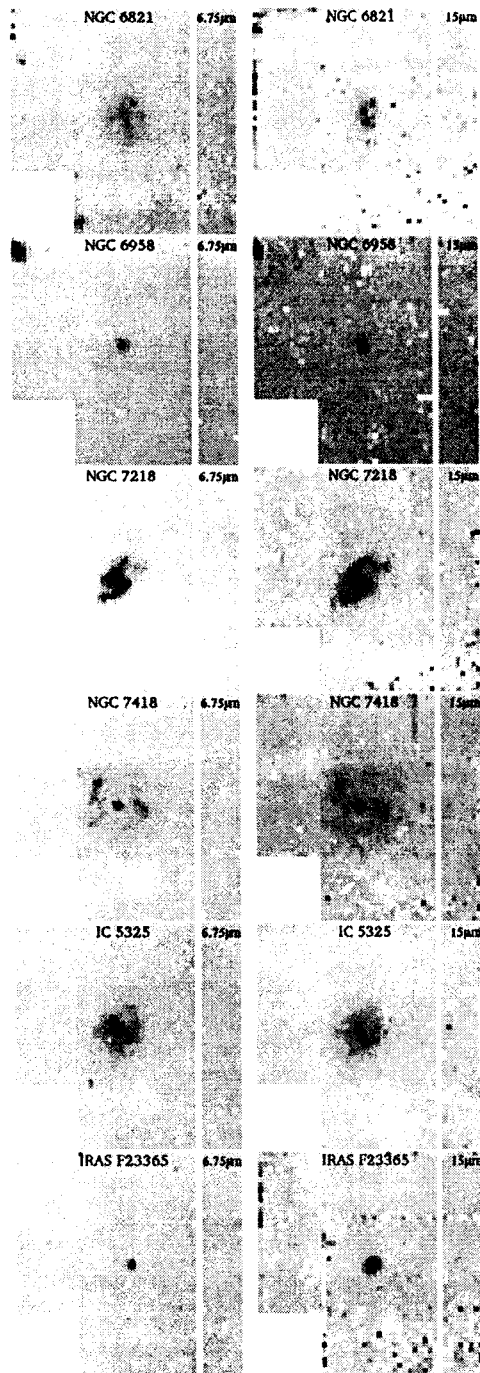
NGC 7418 DSS



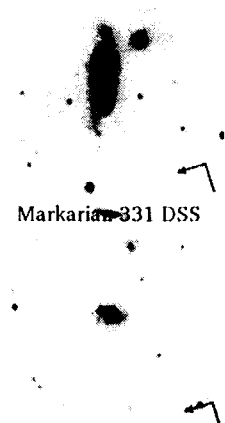
IC 5325 DSS



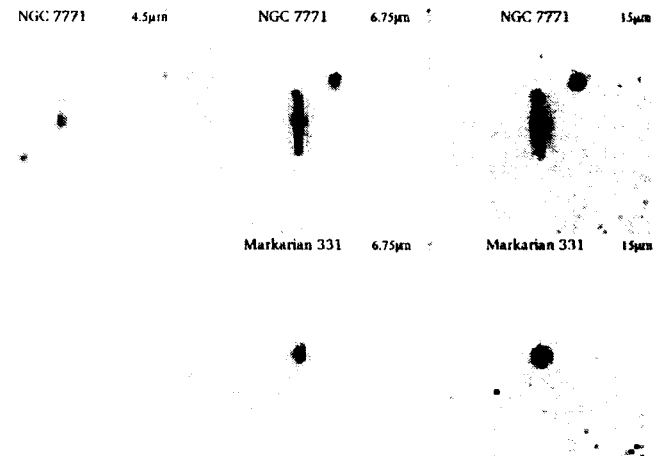
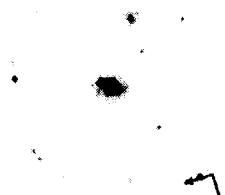
IRAS F23365 DSS

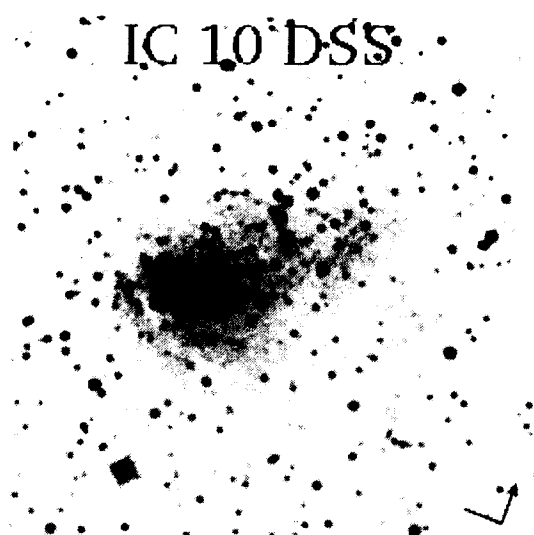


NGC 7771 DSS

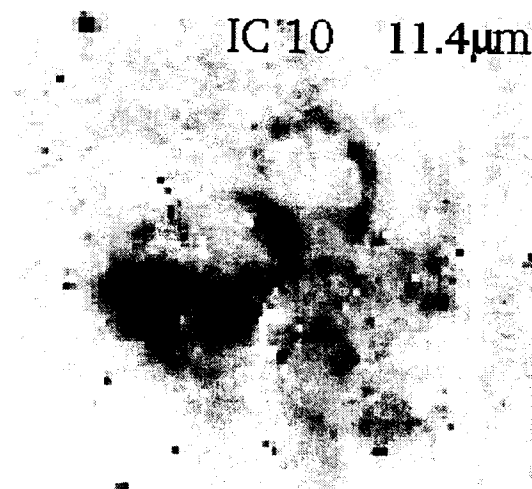
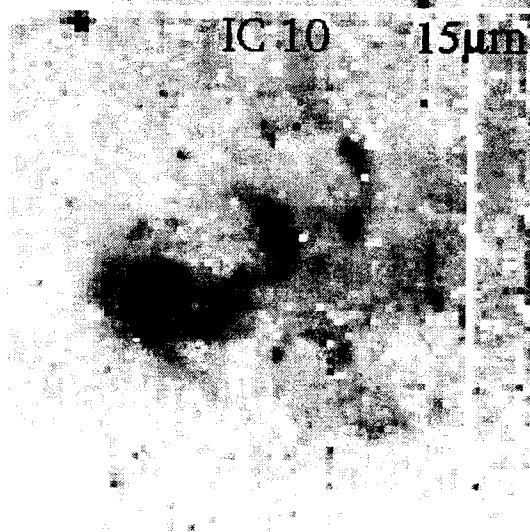
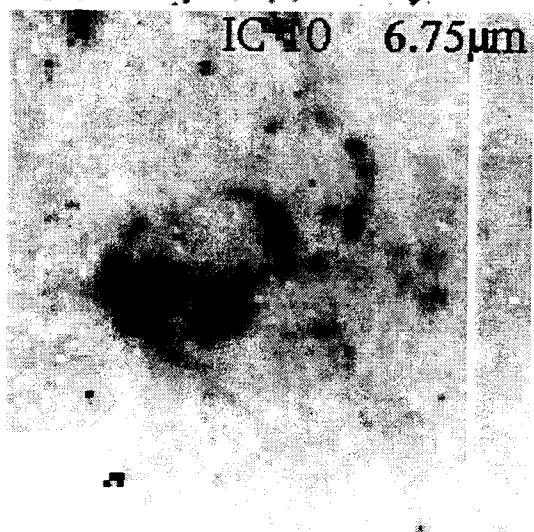
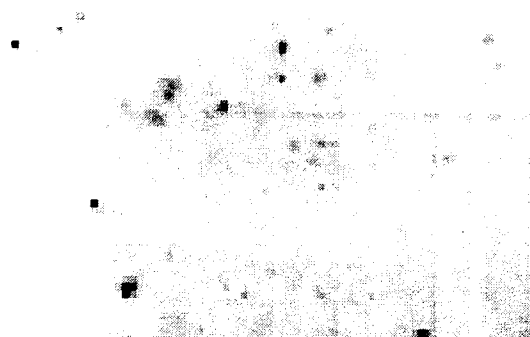


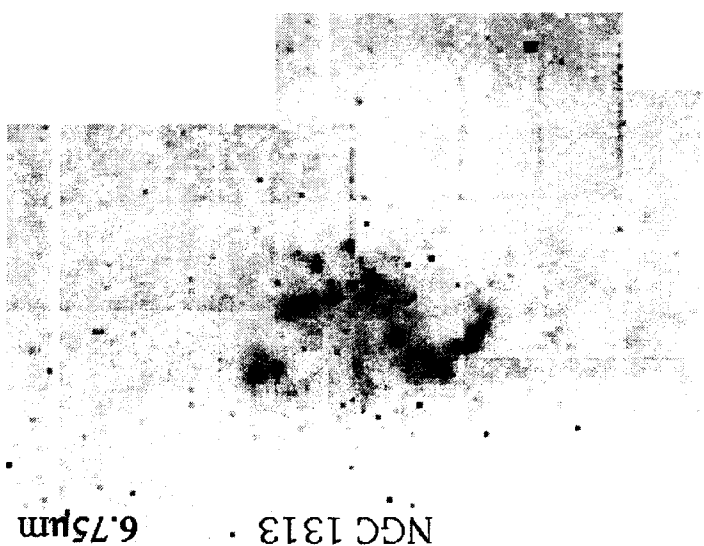
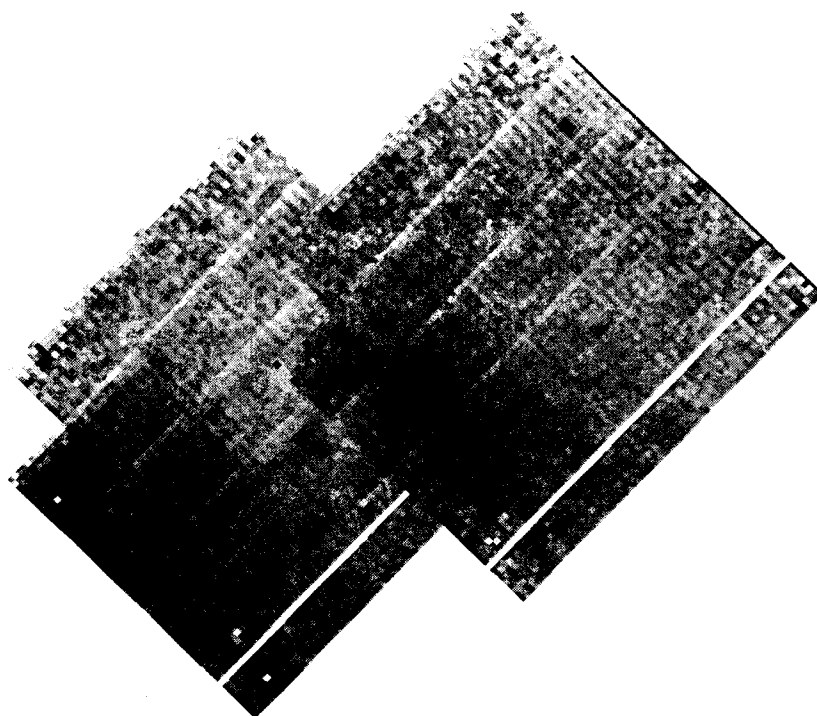
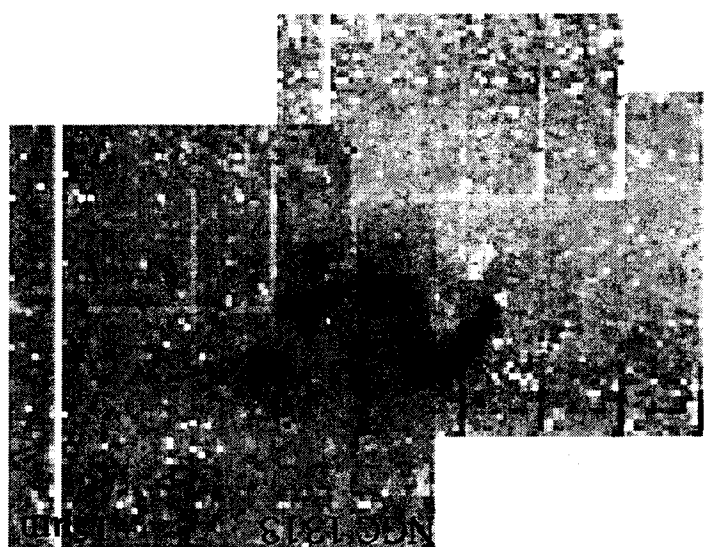
Markarian 331 DSS



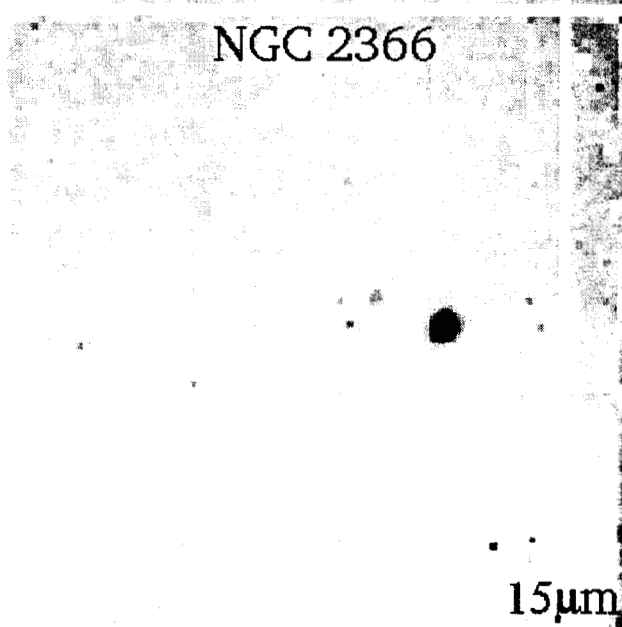
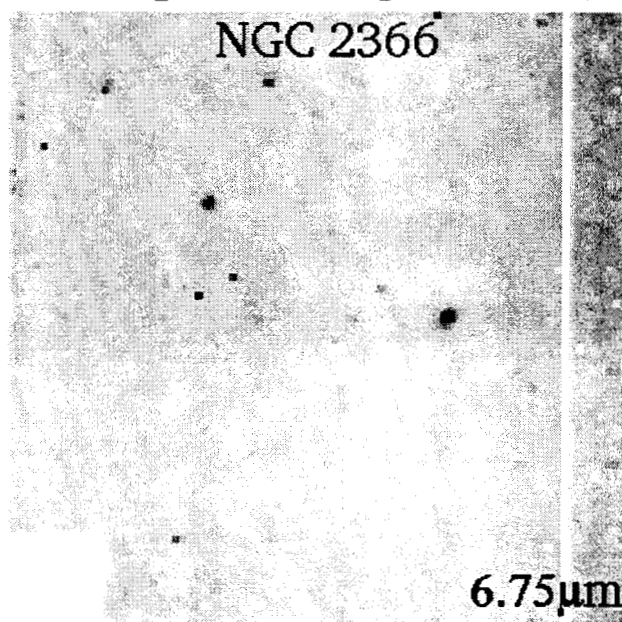
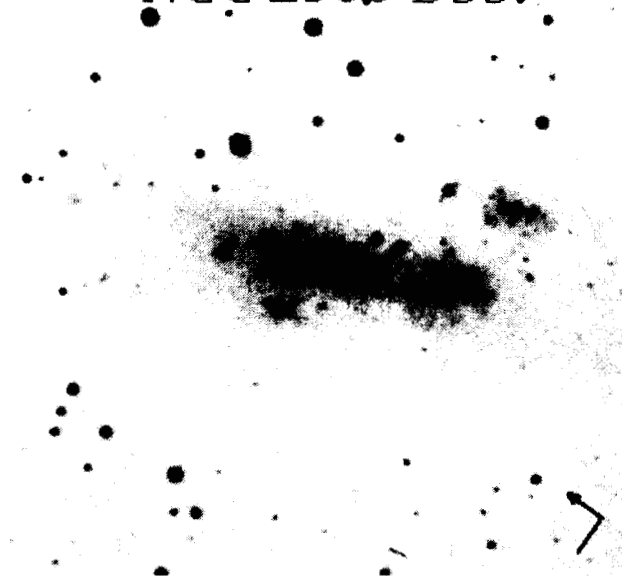


IC 10 4.5 μ m

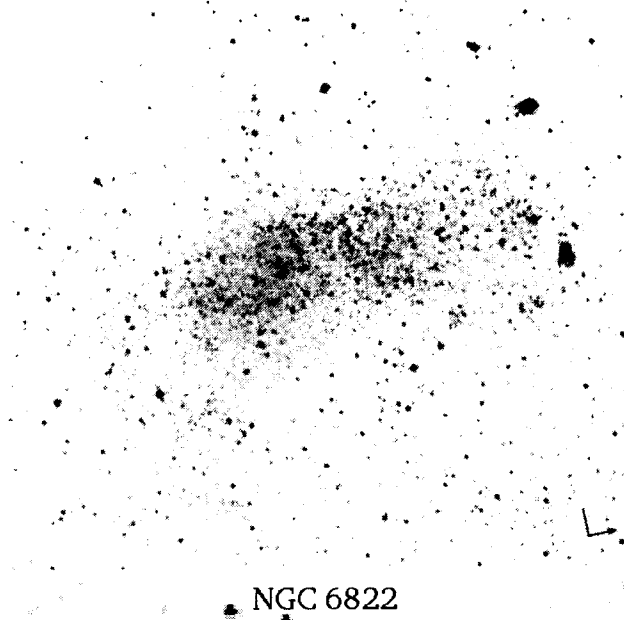




NGC 2366 DSS.

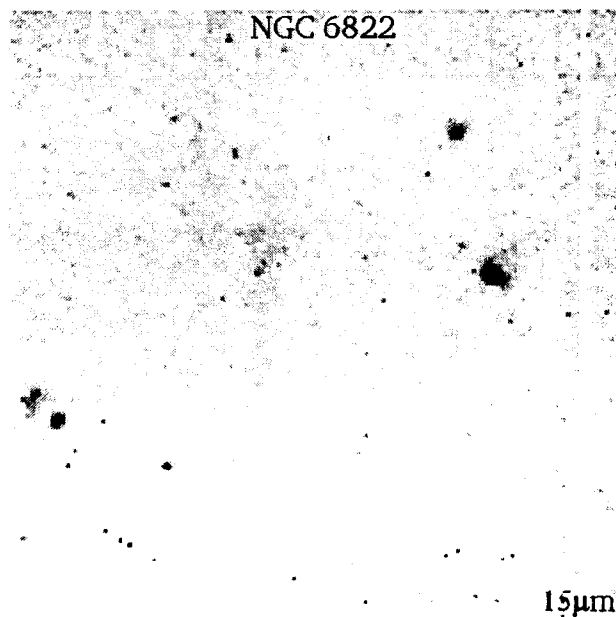


NGC 6822 DSS



NGC 6822

6.75 μ m



NGC 6822

15 μ m

